Structural and chemical ordering of Heusler Co_{x}Mn_{y}Ge_{z} epitaxial films on Ge (111): Quantitative study using traditional and anomalous x-ray diffraction techniques

B. A. Collins, Y. S. Chu, L. He, D. Haskel, and F. Tsui

Phys. Rev. B **92**, 224108 — Published 14 December 2015

DOI: 10.1103/PhysRevB.92.224108

Structural and chemical ordering of Heusler $Co_xMn_yGe_z$ epitaxial films on Ge (111): quantitative study using traditional and anomalous x-ray diffraction techniques

B. A. Collins,[1, *] Y. S. Chu,[2] L. He,[1, †] D. Haskel,[3] and F. Tsui[1, ‡]

[1] Department of Physics and Astronomy

University of North Carolina, Chapel Hill, NC 27599, USA

[2] National Synchrotron Light Source II

Brookhaven National Laboratory, Upton, NY 11973, USA

[3] Advanced Photon Source, Argonne National Laboratory, Argonne, IL 60439, USA

Abstract

Epitaxial films of $Co_xMn_yGe_z$ grown on Ge (111) substrates by molecular-beam-epitaxy techniques have been investigated as a continuous function of composition using combinatorial synchrotron x-ray diffraction (XRD) and x-ray fluorescence (XRF) spectroscopy techniques. A high-resolution ternary epitaxial phase diagram is obtained, revealing a small number of structural phases stabilized over large compositional regions. Ordering of the constituent elements in the compositional region near the full Heusler alloy Co_2MnGe has been examined in detail using both traditional XRD and a new multiple-edge anomalous diffraction (MEAD) technique. MEAD involves analyzing the energy dependence of multiple reflections across each constituent absorption-edge in order to detect and quantify the elemental distribution of occupation in specific lattice sites. Results of this study show that structural and chemical ordering are very sensitive to the Co to Mn atomic ratio, such that the ordering is the highest at

---

* Present address: Department of Physics and Astronomy, Washington State University, Pullman WA 99164, USA.

† Present address: School of Electronic Science and Engineering, Nanjing University, China.

‡ Corresponding author.

an atomic ratio of 2 but significantly reduced even a few percent off this ratio. The in-plane lattice is nearly coherent with that of the Ge substrate, while the approximately 2% lattice mismatch is accommodated by the out-of-plane tetragonal strain. The quantitative MEAD analysis further reveals no detectable amount (<0.5%) of Co-Mn site swapping but instead high levels (26%) of Mn-Ge site swapping. Increasing Ge concentration above the Heusler stoichiometry ($Co_{0.5}Mn_{0.25}Ge_{0.25}$) is shown to correlate with increased lattice vacancies, antisites, and stacking faults, but reduced lattice relaxation. The highest degree of chemical ordering is observed off the Heusler stoichiometry with a Ge enrichment of 5 at. %.

PACS #: 61.66.Dk., 68.55.-a, 61.05.C-.

I. INTRODUCTION

Heusler alloys are intermetallic magnetic alloys that contain transition metal elements and an element from the Group 13, 14, or 15 in the periodic table and crystallize in the cubic $L2_1$ and $C1_b$ structures.[1, 2] Many of them exhibit ferromagnetism at high temperatures with large magnetic moments.[2] Interest in these materials grew significantly, since band structure calculations revealed that many of these alloys may be halfmetallic with fully spin-polarized states at the Fermi level and a gap in the minority spin states.[3-6] If realized, half-metals constitute one class of ideal material candidates for solid-state electronic spin filters and injectors.[7] Furthermore, numerous studies have shown [8-11] that thin films of the alloys can be grown epitaxially on a variety of semiconductors and insulators and thus can be integrated into epitaxial heterostructures with these materials for the science and technology of spintronics.[12-14]

Recent observation of nearly 100 % spin polarization in epitaxial thin films of Co_2MnSi using in-situ spin filtered photoemission spectroscopy has further invigorated the research in halfmetallic materials.[15] However, most measurements to date have yielded relatively low spin-polarization in Heusler alloys, about 55 - 60%.[11, 16] The observed low spin-polarization has been attributed to the presence of various structural and chemical disorders, including the lattice site-specific occupation of elemental species. First principles calculations have shown that the presence of the disorders can give rise to impurity states in the minority band gap. The formation of a minority spin gap depends on the strongly hybridized states between ordered sublattices of Co and Mn,[17] and the lack of such ordering could suppress the halfmetallicity. Specifically, in Co_2MnGe and Co_2MnSi, antisites and site swapping between Co and Mn sublattices were shown to have low formation energy leading to impurity states near the Fermi level.[18] Experimentally, neutron diffraction studies on bulk samples have indeed shown the

presence of these chemical disorders.[10, 19, 20] However, the nature of the disorders and their dependence on alloy concentration and synthesis and processing conditions have not been systematically investigated, since such investigations would require a very large number of samples, and in the case of neutron diffraction, each sample would require sufficiently large amounts of materials. As a result, studies completed thus far have employed samples limited to the nominal stoichiometry of the alloys.

In order to elucidate these effects, specifically the interplay between structural and chemical ordering (ordering of elemental species) and spin polarization, it is necessary to develop techniques to examine a large number of samples with different material parameters, such as composition, and to detect and quantify small amounts of the disorders in small amounts of materials, such as epitaxial thin films. Advances in combinatorial synthesis and characterization using molecular-beam-epitaxy (MBE) techniques have made it possible for systematic investigations into the composition dependent properties of ternary alloys, using a small number of thin-film composition-spread samples.[21, 22] MBE growth of the composition-spread sample that contains a large number of alloys on one substrate allows for rapid and systematic characterization of alloys without the unavoidable variations in experimental conditions associated with synthesis, processing, and measurements of numerous conventional uniform samples.

Advanced synchrotron based x-ray microbeam instrumentation and experiments have also been developed for characterizing structure and composition of these samples through x-ray diffraction (XRD) and x-ray fluorescence (XRF) spectroscopy.[23-30] However, conventional charge scattering techniques, including x-ray and electron scattering, are relatively insensitive to the chemical disorders in alloys with comparable atomic numbers and nearly identical bond

lengths between the elements, e.g. Heusler alloys.[10] Among charge scattering techniques only synchrotron-based anomalous scattering (diffraction in the vicinity of an absorption-edge of a constituent element) has shown promise in detecting and quantifying various chemical disorders.[31, 32] In order to realize its potential for quantitative analysis of chemical disorders with high spatial (compositional) resolutions, further development of the technique is necessary, particularly for examining combinatorial composition-spread thin films.

In this article, we report a systematic study of structural and chemical ordering of $Co_xMn_yGe_z$ epitaxial films grown on a single Ge (111) substrate. Dependence on chemical composition has been investigated over the entire ternary compositional space using synchrotron-based microbeam XRD techniques, including crystal structures, 3-dimensional (3D) strain states, and structural phase boundaries. The study shows that a small number of coherent epitaxial structures are stable over a wide compositional range. A multiple-edge anomalous diffraction (MEAD) technique, XRD experiments and analysis versus energy in the vicinities of multiple elemental absorption-edges, has been developed, aimed at determining the quantitative level of element specific ordering at the specific lattice sites. The MEAD technique has been used to examine a smaller compositional region of interest (ROI) near the Heusler stoichiometry of Co_2MnGe. A variety of elemental disorders within the unit cell have been identified and quantified, and their dependences on chemical composition and epitaxial constraints have been examined. Sensitivity and precision at sub-percent levels of the disorders using the MEAD technique have been demonstrated. Our study reveals that the structural and chemical ordering in the Heusler alloy is especially sensitive to the Co-Mn atomic ratio and that the highest ordering occurs off stoichiometry near $Co_{0.46}Mn_{0.23}Ge_{0.3}$.

II. EXPERIMENT

A. Sample and x-ray microbeam techniques

The $Co_xMn_yGe_z$ ternary composition-spread sample was grown using advanced combinatorial MBE techniques that involve sequential deposition of submonolayer wedges of each element along 3 in-plane axes 120° apart, using stepper-motor controlled shadow masks and realtime atomic-absorption spectroscopy (AAS). The growth process is briefly described here, as it has been detailed elsewhere.[21] Prior to the growth of the ternary sample, an atomically smooth Ge (111) surface was prepared through deposition-anneal cycles resulting in a 200 Å thick Ge buffer. Growth of the film was controlled at a rate of 0.1 Å/s and substrate temperature of 250°C, and followed by a 20 minute 450°C anneal, producing an ordered 2D surface near the Heusler stoichiometry as determined by reflection high-energy electron diffraction and scanning tunneling microscopy experiments on samples grown under the same conditions.[22, 33, 34] As shown in Fig. 1, the triangular ternary region of the sample is about 8.8 mm on a side, and has a nominal film thickness of 390 atomic layers, as determined by in-situ AAS measurements and ex-situ XRD experiments and crystal truncation rod (CTR) analysis.[24, 35] Owing to the difference in crystal structures, the film thickness in atomic layers corresponds to different thicknesses at different compositions, e.g. 630 Å at pure Ge and 320 Å at the Heusler stoichiometry. Crosses with a linewidth of ~ 10 μm were scribed on the sample and used as fiduciary marks to correlate the composition of various measurements, resulting in a compositional reproducibility of better than 0.2 at. %.[26]

X-ray studies were conducted at the 2-BM beamline of the Advanced Photon Source (APS) at Argonne National Laboratory. Elliptical mirrors in the Kirkpatrick-Baez geometry were used to focus the beam to ~ 5 μm both vertically and horizontally without chromatic

aberration. This beam size corresponds to < 0.1 at. % compositional spread on the sample with the beam at normal incidence. The sample was mounted on a precision xyz-stage in a Huber 4-circle diffractometer equipped with a NaI point detector with collimating slits for XRD studies and a Si-drift diode energy-dispersive detector for simultaneous XRF spectroscopy experiments to determine sample composition.

The Co and Mn contents of the sample were characterized and quantified using XRF spectroscopy. Each XRF spectrum collected at a given position on the sample was fit using the program MAPS v1.6.3.0 [36, 37] to extract the K_α intensities from each fluorescing element. In order to eliminate many correction factors required for compositional quantification, such as fluorescence yields, air absorption and instrumental effects,[25] the measured intensities were calibrated by using custom deposited polycrystalline thin films of the individual elements as the "standards". The thicknesses of the thin film standards were measured using various techniques, including stylus-based and optical interferometry-based profilometry. The thicknesses were chosen to be close to those of the sample, so the films would have similar XRF backgrounds and self-absorption effects. However, corrections were made for self-absorption (matrix) effects and for the differences in mass density between the polycrystalline standards and the crystalline sample with the measured crystal structure.[26] The resulting uncertainty for the measured film composition, as expressed in elemental areal densities, is estimated to be ~ 1 %, arising primarily from uncertainty in the profilometry measurements of the standards.

A different set of techniques was employed to determine the Ge composition, since the XRF measurement cannot distinguish the Ge atoms within the thin-film from those in the substrate. Film thickness at the pure Ge-apex of the triangular ternary composition region (Fig. 1) was determined using CTR analysis of the coherent interference fringes in XRD between

the surface and interface.[24, 35] The location of the zero-Ge composition boundary of the triangular region opposite the Ge apex was located using various depth sensitive probes, including energy-dispersive x-ray (EDX) spectroscopy and dynamic secondary-ion mass spectrometry (SIMS), by tracking the Ge signals along the Ge deposition profile. The location was further confirmed by the evolution of the film's lattice constant determined by XRD. From these, a linear Ge thickness profile was determined and combined with those of the Mn and Co to produce a composition versus position map/grid on the substrate, as shown in Fig. 1(a). We note that in principle it is possible to measure the Ge content within the film by grazing incidence (below the critical angle) XRF experiments, but these experiments have many constraints and limitations, including large x-ray footprints, so they were not performed for this study.

The magnetic properties of the ternary sample were studied using magnetooptical Kerr effect (MOKE). Both DC imaging MOKE and scanning MOKE were performed as a function of temperature, using a stabilized diode laser (at 664.3 nm) and a Joule-Thomson refrigerator, primarily in a longitudinal geometry using *s*-polarized light, as detailed elsewhere.[38, 39] For imaging MOKE, the light was expanded and collimated, and the detection was done using a 12-bit digital camera. For scanning MOKE, the light was focused, and the sample was scanned with respect to the laser spot using a precision sample stage. The signal was modulated using a photoelastic modulator and detected using lock-in techniques for simultaneous detection of the Kerr ellipticity and rotation. The MOKE intensity was normalized by the reflectance.

B. X-ray diffraction, crystallographic coordinate systems and transformation

Traditional XRD experiments were performed at 10.5 keV, sufficiently away from the absorption-edges of the constituent elements, in order to study the crystalline structures and map out the structural phase diagram. Earlier studies [23, 33] have shown that epitaxial films of

$Co_xMn_yGe_z$ grown on Ge (111) exhibit either hexagonal or cubic structures depending on the composition. For this study, our approach is to take short reciprocal space x-ray scans that are sensitive to the two structures (the rapid screening as detailed below) in order to locate the structural phases and phase boundaries with high compositional resolution, and to combine this with a full crystallographic study within each identified phase, since it is impractical to do the latter at a high compositional resolution.

In order to conveniently express the structure of the film, especially its epitaxial relationship with the substrate and anisotropic lattice distortions, a hexagonal surface coordinate system was used.[40] In this coordinate system, the a- and b-axes are parallel and c-axis is perpendicular with respect to the substrate surface, as shown in Fig. 2. The extended unit cell for the Ge substrate is represented as a hexagonal structure with the respective parallel and perpendicular lattice parameters, $a = a_0/\sqrt{2}$ and $c = \sqrt{3}a_0$, where a_0 is the cubic lattice constant of Ge (5.658 Å). Consequently, the reciprocal space of the Ge substrate can be indexed using the hexagonal indices of the sample reference frame, $(HKL)_h$, which are related to the conventional cubic indices, $(hkl)_c$ through the coordinate transformation matrices given by

$$\begin{pmatrix} H \\ K \\ L \end{pmatrix} = \begin{pmatrix} -1/2 & 1/2 & 0 \\ 0 & -1/2 & 1/2 \\ 1 & 1 & 1 \end{pmatrix} \begin{pmatrix} h \\ k \\ l \end{pmatrix}, \text{ and } \begin{pmatrix} h \\ k \\ l \end{pmatrix} = \begin{pmatrix} -4/3 & 2/3 & 1/3 \\ 2/3 & 2/3 & 1/3 \\ 2/3 & 4/3 & 1/3 \end{pmatrix} \begin{pmatrix} H \\ K \\ L \end{pmatrix}. \quad (1)$$

The subscripts h and c are used to specify the respective hexagonal (UPPERCASE) and cubic (lowercase) indices. Several examples of the conversion are shown in Fig. 2. The magnitudes of the out-of-plane and in-plane reciprocal space vectors are $|q_\perp| = (2\pi/c)L$ and $|q_{||}| = (2\pi/a)\sqrt{4(H^2 + HK + K^2)/3}$, respectively.

The diffraction patterns for the diamond structure from the substrate (black circles in Fig. 2) were used as a set of references in reciprocal space to scale the film reflections, and the lattice parameters of the film were obtained with respect to those of the substrate. For a cubic lattice, the film's in- and out-of-plane lattice parameters are given by $a' \equiv (K/K')a$ and $c' \equiv (L/L')c$, respectively, whereas for a hexagonal lattice, the corresponding lattice parameters are $a' \equiv (K/K')a$ and $c' \equiv (L/2L')c$. Here, the primed and unprimed parameters correspond to those of the film and the substrate, respectively. The pattern of reflections along each *L*-rod in reciprocal space is determined by the specific atomic stacking. The diamond and face-centered cubic (FCC) structures both have 3-fold symmetry about the $\langle 111 \rangle_c$ axis and obey an ABC stacking sequence. A 60°-twin can arise and its reflections are indexed with an asterisk, as shown in Fig. 2 (the blue open circles). In contrast, the hexagonal structure has equally spaced patterns along all *L*-axes and at even values of *L*, owing to the AB stacking sequence (red circles in Fig. 2). The crystallographic phases of the film were determined using this difference in the symmetries of the diffraction patterns.

When the relaxed lattice constant of film or the literature value is known, a_0' for a cubic structure, and a_0' and c_0' for hexagonal, the respective out-of-plane and in-plane strains are given by

$$\varepsilon_\perp = \frac{c' - \sqrt{3}a_0'}{\sqrt{3}a_0'}, \text{ and } \varepsilon_\parallel = \frac{a' - a_0'/\sqrt{2}}{a_0'/\sqrt{2}}, \text{ for cubic structures, and}$$

$$\varepsilon_\perp = \frac{c' - c_0'}{c_0'}, \text{ and } \varepsilon_\parallel = \frac{a' - a_0'}{a_0'}, \text{ for hexagonal structures.} \quad (2)$$

If the film is fully elastic, the strains are related through the effective Poisson's ratio, $\varepsilon_\perp = -\nu\varepsilon_\parallel$.

The following procedure was employed to map the phase diagram of the ternary combinatorial sample. First, a short, out-of-plane (L) scan of the $(014)_h$ reflection was completed, as this region contains reflections from both the FCC* and hexagonal structures (the box in Fig. 2). This scan minimizes angular movements required at each location on the sample, and the reflection has a smaller beam footprint on the surface due to the higher incident angles relative to the other reflections investigated. Additionally, the absence of a nearby strong substrate Bragg reflection enabled accurate measurement of much weaker diffraction intensities from the thin-film. These scans were acquired in a positional mesh on the ternary sample corresponding to the composition dependence. Results reported in this article correspond to a composition ROI between 10 and 60 at. % of Ge and all combinations of Co and Mn (the trapezoidal region in Fig. 1), including the two binary regions of Ge-Co and Ge-Mn. The measured diffraction intensities versus momentum transfer wavevector $\boldsymbol{q}$ (q-vector) were then fit to Voigt functions to obtain integrated intensity, L-position, and full-width-at-half-maximum (FWHM) for each diffraction peak. The nature of structural phases and phase transitions were examined as a function of sample position (composition).

C. Anomalous x-ray diffraction experiments and analysis

Full Heusler alloys crystallize in the $L2_1$ structure, which consists of four interpenetrating FCC sublattices.[2] For Co_2MnGe, Ge atoms occupy one of the FCC sublattices (the A-sites), Mn another one (the B-sites), while Co occupy two of the remaining two sublattices (the C-sites), as shown in Fig. 3. The $L2_1$ crystal structure produces three unique families of Bragg reflections: one "fundamental" (F) and two "superstructure" (S1 and S2) reflections. These reflections and their attributes are listed in Table I. The fundamental reflection is insensitive to chemical disorders, as its structure factor is the sum of the atomic form factors for all sites in the unit cell,

whereas the superstructure reflections involve differences of the sublattice form factors. The differences within the structure factors give rise to diffraction intensities that depend sensitively on the chemical ordering of the lattice. For example, if the elements in the Heusler alloy were to randomly occupy the sites in this structure, the structure factors in the S1 and S2 reflections would add to zero and the diffraction intensity would vanish.

The anomalous XRD technique involves diffraction as a function of incident photon energy through a characteristic absorption-edge of an element, so it can provide elemental sensitivity to ordering of multiple constituent atoms within the lattice structure. Since the material system under investigation consists of three different elements, our investigation spanned over three absorption-edges. A three-step procedure was employed to obtain the diffraction intensity as a function of energy or "energy-scan". First, the peak center of a given reflection was determined by acquiring in-plane ($q_{\parallel}$) and out-of-plane ($q_{\perp}$) scans at a given energy. Second, an energy-scan with a fixed *q*-vector was carried out to measure the energy-dependent peak intensity. The angles of the diffractometers were adjusted for each energy point, in order to maintain the constant value of *q*. Third, after the completion of each energy-scan, the in-plane and out-of-plane *q*-scans were performed at the final energy to confirm that the peak intensity was properly tracked during the energy-scan. XRF background in the diffraction signal was also measured and removed by positioning the diffractometer away from the Bragg reflection and conducting a separate energy-scan.

For quantitative analysis of the site-specific disorders, energy-scans were acquired over several hundred eVs around each element's K absorption-edge (i.e. Co, Mn, Ge) and at each unique Bragg reflection (Table I). For each energy-scan, the diffraction intensities were subsequently scaled by the corresponding *L*-scan integrated intensities (i.e. $q_{\perp}$-scans) acquired at

pre-edge and post-edge energies, assuming a constant peak width (see discussion below), as shown in Fig. 4(a). Once scaled, the three energy-scans for a particular Bragg reflection were combined into one spectrum for quantitative analysis, as shown in Fig. 4(b). The widths of the Bragg reflections at the energies shown in Fig. 4(a) were further characterized by the $q_{\perp}$, $q_{\parallel}$, and azimuthal (ϕ) rocking-scans. These experiments show that the widths did not change significantly with energy at the compositions investigated, and thus demonstrate that the method described above for extracting the full integrated intensity versus energy was adequate without the need of continuous rocking scans, as these were done in a previous study.[31] Further supporting the method used is the fact that the diffraction intensities of the energy-scans, when scaled by the integrated *L*-scan below the edge, match those scaled by the corresponding counterparts above the edge. Additionally, the scaled energy-scans "line-up" very well at energies away from any resonances/edges [at 9.0 and 10.5 keV in Fig. 4(b)] exhibiting a smooth continuous trend over the entire measured energy range (6.4 to 11.3 keV) as expected. Near each absorption edge and for each Bragg reflection, the diffraction intensity exhibits a unique energy dependent resonance feature. *It is this feature that is sensitive to the chemical ordering within the unit cell*.

The energy (*E*) dependent diffraction intensity can be modeled as follows:

$$I_{\boldsymbol{q}}(E) = I_0(E)\left|\sum_n \left[C_n f_{\mathrm{Co}}(\boldsymbol{q},E) + M_n f_{\mathrm{Mn}}(\boldsymbol{q},E) + G_n f_{\mathrm{Ge}}(\boldsymbol{q},E)\right]\exp\left(i\boldsymbol{q}\cdot\boldsymbol{r}_n - \sigma^2 q^2/2\right)\right|^2 \cdot T(\boldsymbol{q})\,A(\boldsymbol{q},E)\,R(\boldsymbol{q}). \quad (3)$$

Here, within the modulus square is the structure factor of a unit cell, summed over the position $\boldsymbol{r}_n$ of each atomic site (A, B, or C for the Heusler structure). The Debye-Waller factor, which represents random perturbations of the atoms from their equilibrium positions, is parameterized

by the root-mean-square (RMS) deviation σ. The atomic scattering factors $f(\boldsymbol{q},E) = f^0(\boldsymbol{q}) + f'(E) + if''(E)$ comprise of the Thomson scattering factors $f^0(\boldsymbol{q})$ with the real and imaginary anomalous corrections, $f'(E)$ and $f''(E)$, respectively. These factors were modeled using the algorithm developed by Cromer and Liberman.[41] They were corrected for solid-state effects at the Co- and Mn-edges using extended x-ray absorption fine structure (EXAFS) measurements acquired simultaneously with the diffraction data via XRF, and at the Ge-edge using *ab initio* calculations (i.e. the FEFF8 software package).[42] The corresponding coefficients C_n, M_n, G_n are the respective Co, Mn, and Ge elemental occupancies for each site n. The energy-dependent correction factor $I_0(E)$ includes detector efficiencies, air absorption, and energy-dependent response from the beamline optics, while the $\boldsymbol{q}$-dependent correction factors, $T(\boldsymbol{q})$, $A(\boldsymbol{q},E)$, and $R(\boldsymbol{q})$ correspond to the geometric photon path length through the film, absorption of the film, and instrument resolution function correction, respectively.

The photon path length and absorption were calculated from known diffraction geometry and film composition. The resolution function correction for the integrated rod-scan was modeled using the detector slit geometry convoluted with a 3D Lorentzian ellipsoid in reciprocal space to represent the actual Bragg reflection. For this correction, the effect of the detector slit geometry was by far the most important as it was at least ten times larger than that of the incident beam divergence or the energy dispersion. For the Debye-Waller factor, a scalar RMS deviation σ was measured by comparing the intensity of multiple orders of the same Bragg reflection. Details of how these correction factors were calculated and how their accuracies were tested can be found in Ref. 26.

The measured intensities were fit to Eq. (3) using the Levenberg–Marquardt reduced χ^2-algorithm implemented in IGOR Pro. Prior to the fit, the three energy-spectra that correspond to

the three Bragg reflections [e.g. Fig. 4(b)] were first reduced to two by dividing the intensities of the superstructure reflections by that of the fundamental at each energy. Since the fundamental reflection only depends on the number of unit cells participating in diffraction and is insensitive to chemical ordering, this procedure effectively normalizes the intensities to the total number of unit cells participating in the ordered Heusler structure, thus isolating the information on chemical ordering. This also eliminates the energy-dependent $I_0(E)$ term in Eq. (3), as it is the same for each reflection. In short, the use of the intensity ratios in the fits eliminates the need of any scaling parameters.

The nine occupancy variables in Eq. (3) (C_n, M_n, G_n) were re-parameterized into eight that represents three types of defects/chemical disorders, i.e. site-swapping, vacancies, and antisites, as shown in Table II. At each site, there are three possible constituent elements, one ordered (e.g. Ge in site-A) and two disordered (e.g. Mn and Co in site-A), plus vacancy (i.e. missing atoms from the site). In turn, the percent vacancy at the site is 100 % minus the values of occupancies of the three constituents. The site-swapping parameter corresponds to two elements switching their positions from their respective sites (e.g. Ge from site-A to B and Mn from site-B to A), thus related to the two corresponding disordered occupancy variables (e.g. M_A and G_B). The two occupancy variables are in general not equal, since each is a superposition of the amounts of site-swapping and antisite (excess element from swapping), so the lower (minimum) of the two values corresponds to that of site-swapping. Antisites are different from site-swapping as they change the chemical composition of the model. Therefore, the conversion from occupancy to site-swapping is obtained from the minimum of the two disordered occupancy variables for the two given sites, while the difference of the two variables gives the corresponding antisite parameter. Specifically, the Ge-antisites are excess Ge (>25 at. %)

replacing elements in other sites (i.e. B and C-sites). Ge-antisites were included rather than Mn or Co antisites, because our compositional ROI for the MEAD analysis was for Co:Mn ratio of 2 and Ge ≥ 25 at. %, so there was always more Ge than the number of A-sites.

The best fits were obtained iteratively with a number of constraints. First, the fits were done on intensity ratios in logarithmic scale, thus more evenly weighing the resonance features at the three absorption edges (intensity ratios typically varied by two orders of magnitude). Second, the model can only determine the relative values of the three vacancies owing to correlations between the parameters, so we set the site (B-site) with the lowest initial fit value to zero for subsequent fits, thus reducing the total number of fit parameters to 7. The lowest vacancy value was self-consistently checked against the results from the analysis, particularly those for the second lowest vacancies (A-site) and the uncertainties. Third, the output composition from the fits was constrained to the measured nominal composition, particularly the Ge content. Finally, the Debye-Waller σ factor included in the analysis was a scalar but in general can vary with crystallographic direction [Eq. (3)]. Thus measurements of this factor using different pairs of reflections resulted in different values ranging between 0.1 and 0.25 Å. Therefore, a series of fits were performed by systematically varying σ and noting the composition and χ^2 value output from the fit. For each diffraction spectrum, one σ value yielded both the best Co:Mn atomic ratio (closest to the nominal value for a given composition) and the lowest χ^2 value and thus was used for the final analysis. Once the appropriate parameter values were chosen and the constraints were in place, a wide range of starting values for the various chemical disorders was used to fit each spectrum to check for uniqueness and correlations. These effects are discussed in Sec. I of Supplemental Material [].

III. RESULTS AND DISCUSSION

A. Epitaxial phase diagram

Structural phases, phase transitions, and stain states have been studied as a function of composition using traditional XRD. We first present the results from out-of-plane *L*-scans through the $(014)_h$ reflection (Fig. 2 and Table I), starting with two characteristic compositional line-scans to describe features in the structural phase diagram, in order to guide the subsequent presentation of the ternary compositional ROI (the trapezoidal region in Fig. 1) and the smaller ROI centered around the Heusler stoichiometry (the rectangular region in Fig. 1). The diffraction intensities along with the integrated intensity, position and width of the Bragg peak for a constant Ge concentration through the Heusler stoichiometry Co_2MnGe, i.e. $(Co_xMn_{1-x})_{0.75}Ge_{0.25}$, and a constant Co:Mn ratio of 1, i.e. $(CoMn)_{1-y}Ge_y$, are shown in Figs. 5 and 6, respectively. As described above, the $(014)_h$ reflection is insensitive to chemical disorders (Table I) and since the elemental form factors change very little, the integrated diffraction intensity provides a direct measure for crystalline order. Furthermore, the peak position of $(01L)_h$ is indicative of the type of crystalline structure (Fig. 2), and when this is combined with further XRD experiments and analysis, the structural phases have been determined (labeled in Figs. 5 and 6). We note that when discussing in-plane lattice parameters we use the term "coherent epitaxy" to indicate a' being the same as a of the substrate but the term "lattice matched" to indicate the relaxed in-plane lattice parameter of the film matching that of the substrate.

1. Compositional line-scans

As shown in Fig. 5, there are two dominant structures along the compositional line of $(Co_xMn_{1-x})_{0.75}Ge_{0.25}$, a cubic structure on the Co-rich side (labeled as Cubic 1 for $x > 0.5$) and a hexagonal structure on the Mn-rich side (Hex 1 for $x < 0.5$). Near the two Ge-binary regions,

there are two additional phases with weak diffraction intensities, one labeled as Cubic 2 near Co_3Ge and another labeled as Hex 2 near Mn_3Ge. The diffraction intensity for the main cubic structure (Cubic 1) exhibits a sharp maximum at the Heusler stoichiometry of 50 at. % Co (Co:Mn ~ 2), which is accompanied by a maximum integrated peak intensity and a minimum in the corresponding FWHM for the diffraction peak [red diamonds and lines in Figs. 5(b) and (c)]. The integrated intensity drops to half of the maximum value roughly 1 (4) at. % below (above) the Heusler stoichiometry. The out-of-plane lattice parameter of the film, c', at the Heusler stoichiometry is about 2.2 % larger than that of the substrate [Fig. 5(a)], consistent with the bulk value.[2] At a higher Co concentration (~60 at. % Co or Co:Mn ~ 4), the integrated intensity exhibits a local maximum with a corresponding minimum in the FWHM. Here, the c' matches that of the substrate (i.e. $c' = c$). Away from this range of concentrations (50-60 at. % Co), the diffraction intensity decreases with the increased peak width indicating reduced crystalline ordering. Similarly, the behaviors for the main hexagonal structure (green circles and lines in Fig. 5) exhibit a broad maximum in the integrated intensity centered around 45 at. % Mn.

By far the highest diffraction intensity along this line of composition belongs to the film at the Heusler stoichiometry, almost 2 times higher than those at other compositions [Fig. 5 (b)]. The combination of high diffraction intensity and narrow FWHM indicates that the film at this composition has the highest crystalline quality with long structural coherence length, and the ordering is very sensitive to the concentration. A Scherrer analysis of the peak width at this composition after removing considerable instrumental broadening effects yields a coherence length along the film normal approximately equal to the film thickness. The cubic structure that is lattice matched with the substrate at ~60 at. % Co (or Co:Mn ~ 4) and Hex 1 structure over a wide range of concentrations are also highly ordered. In contrast, Cubic 2 and Hex 2 are

disordered structures. The boundaries between the structural phases exhibit discontinuous changes in the out-of-plane lattice parameter (*L*-position), where two diffraction peaks with low intensities and high FWHM coexist over a significant range of concentrations (~10 at. %). In other words, the phase boundaries across this range of compositions are characterized by coexistence of two disordered structures.

At a constant Co:Mn ratio of 1, along a compositional line perpendicular to the one discussed above, two hexagonal phases, Hex 1 and 3, have been identified, as shown in Fig. 6. The diffraction intensity exhibits a broad maximum centered around 50 at. % Ge, where the FWHM of the diffraction peak exhibits a local minimum. Here, the most ordered phase is Hex 3. The *L*-position (out-of-plane lattice parameter) varies continuously, which is different from the discontinuous behavior described above. Instead, the structural phases are separated by maxima in the peak width at 42 and 57 at. % Ge (dashed lines in Fig. 6). The out-of-plane lattice parameter for the Hex 1 structure is nearly constant (~5.38 Å), while the counterpart for Hex 3 changes approximately linearly. The former is comparable to the c-axis spacing of 5.32 Å of a known hexagonal alloy, CoMnGe.[43] Unlike the sharp peak at the Heusler stoichiometry, the diffraction intensity does not show any discernable composition dependent feature around CoMnGe [arrows in Figs. 6(b) and (c)]. The structures above 57 at. % Ge were not studied in this work.

2. Ternary phase diagrams

We now turn to the XRD results for the ternary ROI (the trapezoidal region in Fig. 1). Figure 7 shows the ternary compositional maps for the out-of-plane Bragg peak position [*L*-position through $(014)_h$], integrated intensity of the peak, and its FWHM. The composition grid was determined experimentally, as described in Sec. II.A. In compositional regions where two

diffraction peaks coexist, i.e. discontinuous boundaries, results for Bragg peaks with the higher integrated intensity are shown. The *L*-position map [Fig. 7(a)] shows two primary discontinuous boundaries in composition, along two approximately constant Co:Mn ratios of 1:4 and 3:2, thus dividing the maps into three regions, Co-rich, "center", and Mn-rich. As discussed above, a discontinuity in *L*-position and a high FWHM are indicative of a phase boundary, whereas films with a high diffraction intensity and a low FWHM correspond to highly ordered structures.

We start with the Co-rich region of the maps. This region contains cubic structures with the highest XRD intensities within the entire ternary ROI, accompanied by the narrowest FWHM. The compositions of these "high intensity" structures are located primarily between 25 and 55 at. % Ge and along two constant Co:Mn ratios of 2 and 4 (the dash-dotted lines in Fig. 7). The highest integrated intensity forms a narrow "ridge" in composition along Co:Mn = 2 with a corresponding "valley" in FWHM. Along the intensity-ridge, the *L*-position is approximately 3.9 rlu, or $(c'-c)/c$ of ~2.2 %, and the diffraction intensity increases monotonically with Ge concentration, reaching a maximum at ~50 at. % Ge. The diffraction intensity exhibits a local maximum in composition along Co:Mn = 4, where the FWHM is at a local minimum and the lattice parameter of the film with *L*-position = 4.0 rlu matches that of the substrate.

Near and within the Co-Ge binary, the diffraction intensities exhibit two broad peaks that overlap with each other. The more intense of the two (parameters shown in Fig. 7) is also the narrower one with a relatively constant $(c'-c)/c$ = + 5.3(2)% or 4.2 rlu. The less intense peak (not shown) has a very wide FWHM of 0.20(1) rlu, but with $(c'-c)/c$ = + 2.2(2)%, the corresponding structure is better lattice-matched with Ge. The presence of the two diffraction peaks indicates coexistence of two cubic structures in this sub-region, which is separated from the main cubic structure (Cubic 1) by a peak in FWHM [Figs. 5(c) and 7(c)]. The multiple

structures combined with low diffraction intensities and wide FWHM indicate that the films within this compositional region are disordered.

The compositional region in the center of the ternary diagram between the two main *L*-position discontinuities [Fig. 7(a)] contains hexagonal structures with the *L*-position centered around 3.6 rlu. Within this region, the peak parameters exhibit similar dependence on Ge concentration as those for Co:Mn = 1 (Fig. 6). Specifically, there are two sub-regions of phases, separated primarily by a peak in FWHM near 50 at. % Ge. The highest diffraction intensities in this region occur above 50 at. % Ge with the maximum intensity and minimum FWHM near $Co_{0.18}Mn_{0.27}Ge_{0.55}$. Below 50 at. % Ge, there are three minimum FWHM "valleys" along constant Co:Mn ratios of approximately 1:1, 3:4, and 2:5 [dashed lines in Fig. 7(c)], accompanied by a broad maximum in *L*-position and intensity along Co:Mn ~ 3:4. At each of these compositions (constant Co:Mn ratios), the hexagonal out-of-plane lattice parameter, c' is relatively constant, and their respective values are 5.38(1), 5.36(1), and 5.49(1) Å. These features are discernable in the compositional line scan shown in Fig. 5 (the green circles and lines), including the plateaus in *L*-position (c') at these compositions [Fig. 5(a)].

In the Mn-rich region, especially within the Mn-Ge binary, the structure is hexagonal, and the *L*-position is nearly constant, which corresponds to a c' of 5.10(2) Å. A separate in-plane measurement of the peak revealed that a' = 4.17 Å, with a significant lattice mismatch with the substrate. Throughout this region, the diffraction intensities are relatively constant and are 1-3 orders of magnitude below those of other phases, consistent with low ordering, and perhaps more precisely, small fractions of ordered materials within the films.

We note that the region near the Ge-apex (85 – 100 at. % Ge) was also investigated (not shown). No diffraction intensity at the diamond-forbidden $(014)_h$ reflection could be detected.

Instead, interference fringes on the $(10L)_h$ rod near $L = 4$ were observed and they exhibit systematic changes with increasing metal concentration. These findings are consistent with an excellent crystalline order with no stacking faults or twin domains. CTR analysis reveals that the film strains exhibit linear dependence on the concentrations of the two metal elements, thus obeying Vegard's law, similar to the behavior observed in (100) oriented films.[29]

From the XRD results, a ternary structural phase diagram has been constructed, and it is compared with a corresponding magnetic phase diagram, as shown in Fig. 8. As described above, the structural phase boundaries are primarily identified by the maxima in the FWHM of the measured diffraction peak [Fig. 7(c)], which are often accompanied by the local minima in diffraction intensities, and for the *L*-position discontinuities, the coexistence of two diffraction peaks. The main phases described above are labeled in this diagram [Fig. 8(a)], in particular, a cubic phase in the Co-rich region, and three hexagonal phases in the center and Mn-rich regions. The extent of the two-phase coexistence regions is represented in the diagram by striped areas. In contrast, when the *L*-position is continuous, the phase boundaries are represented by dashed lines, e.g. part of the boundaries between Hex 1 and Hex 3, and between Hex 3 and Cubic 1.

The magnetic and magnetooptical properties of the ternary sample were systematically examined in an earlier study.[38] The magnetic phase diagram shown in Fig. 8(b) corresponds to temperature-dependent boundaries/contours of ferromagnetic regions, where saturation MOKE intensities were detected above the detection threshold. Since the boundaries separate regions with and without MOKE intensities, they can be used to approximate the contours of Curie temperature (T_C) versus composition. At 300 K, a large portion of the ternary alloys is ferromagnetic, including all the highly ordered compositions in the Cubic 1, Hex 1 and Hex 3 phases, as discussed above [Figs. 7 and 8(a)]. A large fraction of Cubic 1 region has T_C values

> 470 K, the maximum temperature of the study. The T_C contours are experimentally indistinguishable for temperatures above 350 K, especially for temperatures between 400 and 470 K, where the contours (not shown) are practically identical to each other, indicating a steep rise of T_C at these compositions. This suggests that within this region, T_C is well above the maximum temperature measured, which is consistent with the reported T_C of 905 K for the Co_2MnGe Heusler alloy (white dots in Fig. 8).[2, 19]

The T_C contours show correlation with significant portion of the structural phase boundaries, including the one between Cubic 1 and Hex 1, and those around Hex 3. Near the boundary between the Cubic 1 and Hex 1 lies a region with T_C between 350 and 400 K, which contains a known hexagonal structure of CoMnGe (orange dots in Fig. 8) with a reported T_C of 390 K.[44] In addition, the MOKE intensities exhibit strong correlation with structural ordering, as shown in Fig. 8(b) for the room temperature behavior in the remanent state (at zero-field after saturation). Specifically, high remanent MOKE intensities are observed along approximate Co:Mn ratios of 2:1, 1:1, 3:4, and near $Co_{0.18}Mn_{0.27}Ge_{0.55}$, where high structural ordering is also observed (Fig. 7). Evidently, the compositions at Co:Mn near 4:1 and 2:5 are not ferromagnetic at room temperature. The saturation MOKE intensities (not shown) exhibit qualitatively the same behavior. Upon closer examination, the MOKE intensities exhibit a step across Co:Mn = 2, and a resonance-like anomaly centered around 45 at. % Ge that coincides the "fist-like" feature at the boundary between Cubic 1 and the Cubic 1-Hex 1 two-phase region [in the middle of Fig. 8(a)]. The former change has been determined to be the result of the corresponding changes in magnetic anisotropy and magnetooptical coefficients at this composition.[38, 39]

The results shown in Figs. 7 and 8 reveal that a high-quality epitaxial film with a few crystalographic structures has been stabilized over nearly the entire ternary composition space by

the low temperature non-equilibrium MBE growth. In contrast, a similar study of $Co_xMn_ySi_z$ growth on Ge (111) [30] shows that under similar growth conditions, high quality epitaxial growth occurs only in the cubic Co-rich region (> 45 at. % Co) and otherwise the film is largely nanocrystalline. The presence of a stable room temperature hexagonal structure in the germanium-based Mn-rich system and the absence of such hexagonal phase at room temperature in the silicon-based system are evidently responsible for the very different results. In the latter system, a very stable orthorhombic structure is present in the corresponding compositions.[45] The basal plane of the hexagonal structure is nearly lattice matched with the lattice of Ge (111) surface, while no orientation of the orthorhombic structure is. These findings indicate the important roles played by both epitaxial and chemical constraints.

Bulk ternary Mn germanides and silicides (e.g. CoMnGe and CoMnSi) are orthorhombic at low temperatures, ordered in Co_2P structure, and they transform into hexagonal structures (Ni_2In type) at elevated temperatures via a "diffusionless" process.[45] The difference between the two systems is the transition temperature, with values for the germanides near room temperature whereas those for the silicides > 1000°C. Furthermore, studies have shown that there is significant amount of site swapping between element dependent sublattices in the hexagonal CoMnGe, including elemental site swapping and antisites, and that the structural ordering is relatively insensitive to compositional variations.[44] In other words, the hexagonal germinaides are susceptible to becoming random alloys, particularly when off stoichiometry. We interpret that the observed Hex 1 structure in the Mn-rich region shown in Fig. 8 is derived from these hexagonal germanides. At CoMnGe, our measured c' of 5.38 Å (Figs. 6 and 7) and the coherent in-plane lattice parameter a' of 4.00 Å, when compared to the literature values of 5.32 and 4.07 Å for c_0' and a_0', respectively,[43] correspond to an out-of-plane tensile strain of +1.1% and

an in-plane compressive strain of –1.7% [Eq. (2)]. The resulting Poisson's ratio of 0.65 is quite reasonable for this type of alloys. The aggreement of the measured T_C with that of the bulk alloy further supports this interpretation.

As mentioned above, within the Hex 1 structure, structural ordering and c' are relatively insensitive to Ge concentration. This observation suggests that either the metallic atomic radii for Ge is comparable to those of Co and Mn, or the presence of Co or Mn site vacancies can accommodate the epitaxial constraints. The narrow FWHM in regions along fixed Co:Mn atomic ratios of 1:1, 3:4, and 2:5 indicate higher degree of structural ordering, but the compositions for the latter two ratios do not correspond to any known compounds in the literature, other than the aforementioned CoMnGe germinide. The best structural ordering (high diffraction intensity and low FWHM) in this region is along Co:Mn ratio of ~3:4 away from CoMnGe, and it correlates with high MOKE intensity at room temperature [Fig. 8(b)]. This line of compositions also corresponds to a local minimum in c', which is the closest to the value of c for the hexagonal CoMnGe and thus may correspond to hexagonal alloys with a_0' values that are best lattice matched with Ge (111) surface.

Similarly, the region labeled as Hex 2 [Figs. 5 and 8(a)] appears to be related to the binary compound Mn_2Ge with comparable out-of-pane and in-plane lattice constants (respective bulk values of c_0 = 5.28 Å and a_0 = 4.17 Å).[46, 47] However, the bulk phase is known to exist only at high temperatures (> 790°C). This is consistent with Hex 2 being disordered. In contrast, the Hex 3 structure does not correspond to any known alloy,[43, 48] but it is ferromagnetic at room temperature and contains highly ordered structures, including the highest ordering within the hexagonal phases studied near the composition of $Co_{0.18}Mn_{0.27}Ge_{0.55}$ or roughly $Co_2Mn_3Ge_6$.

Again, the maximum diffraction intensity and narrowest FWHM correlate well with high MOKE intensity (Figs. 7 and 8).

In the two-phase boundary region between Cubic 1 and Hex 1, several known bulk hexagonal compounds were not detected, including Co_3Mn_2Ge and $Co_4Mn_3Ge_6$ with resepctive a_0 values of 4.803Å and 5.081Å.[43] This observation is likely the result of the large lattice mismatch between these structures and the Ge substrate.

Thermodynamics of the Heusler alloy appears to play an important role in the Cubic 1 region, where alloys along Co:Mn = 2 with about 2% lattice mismatch exhibit a higher level of ordering compared to the lattice matched counterparts at Co:Mn = 4 (Figs. 5 and 7). The high sensitivity of order to the transition metal atomic ratio suggests that chemical ordering in the Co and Mn sublattices are important for this class of alloys. The Heusler structure is clearly the most magnetic with T_C values well above room temperature, consistent with bulk literature values. Like the hexagonal counterparts, high level of structural ordering in this region also correlates well with high MOKE signal, except for most of Co:Mn = 4, which is not ferromagnetic at 300 K. The observed strong correlations between structural and chemical ordering and MOKE intensity are not surprising, since magnetooptical effects and magnetic anisotropy depend sensitively on spin-orbit interactions that are strongly influenced by the local chemical environment within the lattice. However, this finding provides additional impetus for quantifying these effects.

B. Strain states and structural quality of the cubic structure

We now focus on the smaller compositional ROI centered on the cubic Heusler structure (the dotted rectangular region in Fig. 1), to examine structural ordering and strain states, and to qualitatively assess the chemical ordering within the unit cell. The out-of-plane and in-plane

lattice parameters of the film (c' and a') have been determined from *L*- and *K*-scans, respectively, at both the $(014)_h$ and $(102)_h$ reflections, as shown in Fig. 9. In the ROI, a' is the same (coherent epitaxy) or nearly the same as that of the substrate, with $(a'-a)/a$ < 0.5% [Fig. 9(b)]. Specifically, the in-plane lattice parameter of the film is fully coherent with that of the substrate near 50 at. % Ge [the white contour in Fig. 9(b)], and it gradually increases as Ge concentration decreases, to $(a'-a)/a \approx 0.4\%$ ($a' \approx 4.016$ Å) at the Heusler stoichiometry. The latter indicates the presence of some strain relaxation. As Co:Mn ratio increases from 2 to 4, a' also tends toward lattice matching with the substrate. For c', there appears to be two regions [separated by the dashed line in Fig. 9(a)], where the lattice parameter contours are nearly linear and parallel, i.e. linear composition dependence. One region covers compositions of < 50 at. % Ge and Co:Mn ≥ 2, where c' depends mostly on the Co:Mn ratio. Within this region, at Co:Mn = 2, which includes the Heusler stoichiometry, c' is about 10.015 Å (2.2% larger than Ge), whereas at Co:Mn = 4, it matches that of Ge. Using the measured lattice parameters at the Heusler stoichiometry and the literature value for bulk Co_2MnGe (a_0' = 5.743 Å),[2] the corresponding in- and out-of-plane strains are estimated to be –1.1% and +0.69%, respectively [Eq. (2)]. These yield an effective Poisson's ratio of 0.63, which is nearly identical to the one above estimated for the hexagonal CoMnGe. Another region with linear composition-dependence covers the top left corner of Fig. 9(a), nominally > 50 at. % Ge and Co:Mn < 3. The high lattice parameter contours [$(c'-c)/c \geq 5\%$] at Co:Mn ratios < 2 correlate with the aforementioned "fist-shaped" feature at the Cubic phase boundary [middle of Fig. 8(a)]. This second region was not studied in detail.

Assuming that the film is distorted elastically, its relaxed lattice constant can be calculated. For a [111]-oriented system, this involves transformation of a fourth-ranked

elasticity tensor. The cubic symmetry and in-plane biaxial strain reduces this tensor to the scalar relationship given by

$$a_0' = \frac{\left(c'/\sqrt{3}\right) + \sqrt{2}\nu a'}{\nu + 1}, \tag{4}$$

where ν is the effective Poisson's ratio for this orientation (see Sec. II of Supplemental Material [] for the derivation and discussion on ν). In Fig. 10, the relaxed lattice constant calculated using $\nu = 0.6$ and the strain state are shown. The lattice mismatch with Ge is determined from $\varepsilon_0 = \left(a_0' - a_0\right)/a_0$. Since the strains are related through ν, only $\varepsilon_{||}$ is shown in Fig. 10(b). Because a' is either fully or nearly coherent with the substrate over the entire ROI, both the lattice constant and the strain exhibit the same qualitative features as c' [Fig. 9(a)]. Within each of the two compositional regions mentioned above, the lattice constant obeys Vegard's law, i.e. $a_0' = a_{\mathrm{Co}}x + a_{\mathrm{Mn}}y + a_{\mathrm{Ge}}z$ for $\mathrm{Co}_x\mathrm{Mn}_y\mathrm{Ge}_z$, where the coefficients a_{Co}, a_{Mn}, and a_{Ge} are related to the atomic sizes of the respective elements, as they are expressed in cubic lattice constants [e.g. twice the lattice constant of a body-centered cubic (BCC) structure]. The results for the two compositional regions are listed in Table III. For the region with < 50 at. % Ge ($z < 0.5$), the coefficients are consistent with the literature values for the respective lattice constants, specifically for Ge and the BCC structures of the two metal elements.[49-53] For $z > 0.5$ within the large uncertainties due to the relatively small range of compositions analyzed, the Mn coefficient becomes significantly larger, while the Ge and Co counterparts remain roughly the same as those in the region with $z < 0.5$. The lattice constant at the Heusler stoichiometry as in nearly the entire compositional region along Co:Mn = 2, is 5.74(1) Å, corresponding to a lattice mismatch of 1.5(1)% with the Ge substrate, and an in-plane compressive strain of −1.1(2)%. The measured lattice constant is in excellent agreement with the literature value of 5.743 Å.[2]

The composition-dependent intensity maps of all three unique Bragg reflections (Table I) are shown in Fig 11. The integrated intensities of the unique reflections can provide insight into the ordering within the crystal sublattices via their structure factors. For the fundamental F-reflection, the intensity map [Fig. 11(a)] exhibits the narrow ridge of high intensities described above that corresponds to a narrow region of high degree of structural ordering. The intensity ridge is along Co:Mn ratio of 2 below ~45 at. % Ge, and it shifts toward Co:Mn ratio of 2.5 at higher Ge concentrations and reaches a maximum near 50 at. % Ge. The behavior for the S1-reflection is similar to that of the fundamental, but the intensity decreases more quickly with decreasing Ge concentration along Co:Mn = 2 and the maximum intensity is located at a slightly higher Ge concentration, as shown in Fig. 11(b) (for clarity the corresponding intensity line-scans are also shown in Supplemental Material Fig. S1 []). The behavior for the S2-reflection [Fig. 11(c)] has a markedly different composition dependence. While high intensities are still along Co:Mn = 2, they exhibit two maxima near 30 and 40 at. % Ge, without one near 50 at. % Ge. Furthermore, the intensity at this reflection is significantly lower than the other two counterparts. There is no secondary phase detected for Co:Mn ≥ 2 in this ROI.

The intensities of the 60°-twin of the S1-reflection, $(012)_h$ have also been measured as a function of composition, in order to examine the extent of twinning and stacking faults along the out-of-plane [111] direction. This type of reflections is forbidden in the diamond lattice, so both reflections can be measured without interference from those of the substrate. With respect to the substrate, the $(012)_h$ reflection actually corresponds to the FCC-reflection or S1, whereas the $(102)_h$ counterpart actually corresponds to that of FCC* or S1* (Fig. 2 and Table I). In other words, the former has the same stacking as the substrate along [111], while the latter is the 60°-twin of the substrate. By and large within the ROI, the reflection with a higher intensity is S1*

[Fig. 11(b)]. In order to compare the two intensities, a composition-dependent map of the intensity ratio of S1* over S1 is shown in Fig. 11(d). At 50 at. % Ge and Co:Mn ~ 2, near the intensity maxima in both the F- and S1-reflections, the intensity ratio is about 1, indicating that the film consists of 50/50 60°-twins. With decreasing Ge content, the intensity ratio increases, where the film gradually becomes untwined. For Co:Mn ≥ 2, and Ge concentration ≤ 35 at. %, S1 becomes undetectable within the detection limit of the experiment, where the ratio is then calculated by dividing the S1* intensity by the background level [below the red dotted line in Fig. 11(d)], and thus the film has no detectable stacking faults within the detection limit.

In the case of a 50/50 twinning, i.e. the intensity ratio ~ 1, the apparent in-plane six-fold symmetry can easily be distinguished from that of the hexagonal structure, as twinning does not alter the FCC $(00L)_h$ reflections (Fig. 2). It is interesting that the preferred orientation of the film is the 60°-twin of the substrate. This observation is unequivocal since all the reflections from the film at the Heusler composition are sufficiently far from those of the substrate and thus can be measured directly, owing to the large lattice mismatch between the film and the substrate. The 60° rotation appears to initiate at the film-Ge buffer interface, which can be attributed to the nature of the Ge 2×8 surface reconstruction, the same as the growth of Co_2MnSi films on Ge (111).[30]

The four types of intensities shown in Fig. 11 allow us to probe the nature of the ordering as a function of composition. As discussed above, all four intensities near the Heusler stoichiometry exhibit maxima along Co:Mn ratio of 2 (the intensity-ridges), again confirming the general notion that both structural and chemical ordering in this alloy system is very sensitive to the Co:Mn ratio. However, the different intensities exhibit maxima at different Ge concentrations, i.e. “hot spots” at ~ 50 at. % Ge for the F- and S1-reflections, at ~30 and ~ 40 at.

% Ge for S2, and around 30 to 35 at. % Ge for the S1* to S1 ratio. The different hot spots versus composition are the result of the different sensitivity of the measurements to the various types of ordering in the film. One key finding is that in all cases, the maximum intensities are away from the Heusler stoichiometry. While the fundamental gives a direct measure of structural order, the superstructure reflections (S1 and S2) are only present when atoms are organized into the three element-specific sublattices, and the intensities would vanish without such chemical ordering (Table I). These would lead to specific interpretations as follows.

The maximum intensity at the fundamental near 50 at. % Ge indicates where most atoms within the film are ordered in the cubic structure. The high intensity at the S1-reflection is indicative of the C-site being predominantly occupied by Co, i.e. minimum swapping between Co and Mn or Ge. Maximum intensities at the S2-reflection would indicate the best ordering between the Mn and Ge sublattices (A & B sites, respectively), but the overall low intensities of S2 may be the result of significant amount of swapping between the two sublattices. Both S1 and S2 intensities are convoluted by the overall structural ordering (intensity at the F-reflection). At the limit of low-level of chemical disorder with weak concentration dependence, the intensity of S-reflection would correlate with that of F-reflection, as in the case of S1. In contrast, the presence of significant concentration-dependent chemical disorder can suppress the intensity correlation, leading to the different hot spots, as in the case of S2.

The composition-dependent diffraction intensities also exhibit various correlations with the measured strain-states (Figs. 9 and 10). First, the intensity-ridges for the F- and S1-reflections correlate with the contour of the film's lattice parameter, i.e. nearly constant lattice parameter over a large range of Ge content (between 20 and 50 at. % Ge). This observation suggests the presence and systematic change of vacancies, since substituting Ge into Mn and Co

sites (i.e. Ge-antisites) may cause the lattice parameter to change. Second, the highest intensity for the two reflections occurs at where the film is fully coherent in-plane [the white contour in Fig. 9(b)] rather than lattice matched with the substrate [the white contours along Co:Mn ~ 4 in Figs. 9(a) and 10]. Both S1 and S1* exhibit the highest intensity at the same composition [intensity ratio of 1 in Fig. 11(d)], indicating that the most structurally ordered composition is also fully twinned. Furthermore, in the same compositional vicinity, the transition between two different Vegard's laws takes place (Table III), which may signal chemical changes between the two regions, specifically the bonding with Mn and its chemical environment. Furthermore, the observed increase of the Mn bond length appears to be related to the predicted transition from low spin to high spin states in BCC Mn,[54] including the quantitative values of lattice constants for the transition. The presence of stacking faults and twin boundaries and change of chemical bonds may play a role in accommodating the large in-plane strain and keeping the film fully coherent with the substrate. Third, as Ge concentration decreases from 50 at. %, increasing lattice relaxation, suppression of twinning/stacking faults, and presence of chemical ordering all appear to be composition-driven, especially along the aforementioned constant lattice parameter contour, mostly along Co:Mn ~ 2. As one would expect, the diffraction intensity for the F-reflection [Fig. 11 (a)] and thus the structural ordering exhibit anti-correlation with the extent of the in-plane strain relaxation [Fig. 9(b)].

C. Quantifying chemical ordering: anomalous x-ray diffraction

In this section, we present experiments and analysis of anomalous XRD in order to quantitatively probe lattice site-specific substitutional chemical disorders within the cubic ROI around the Heusler stoichiometry. We examine the sensitivity and limitations of this approach in detecting and quantifying various elemental occupancies, starting with results at one absorption-

edge. As mentioned above, previous density functional theory calculations of Heusler alloys indicate that a variety of chemical disorders can destroy the halfmetallic state in this material,[17, 18] but few measurements have been made. The results presented in the previous section indicate that various chemical disorders are indeed present and different chemical ordering may correspond to distinct "hot spots" versus composition different from those of structural ordering. However, the nature of the different hot spots cannot be resolved by using the traditional XRD techniques, and they must be examined and reconciled using techniques sensitive to element specific disorders.

1. Anomalous diffraction at a single absorption-edge

We first examine the diffraction intensity as a function of photon energy across the Co K absorption-edge for the F- and S1-reflections, whose behaviors off-resonance are similar [Figs. 11(a) and (b)], but the contributions from structural and chemical ordering are known to be convoluted. On the Co resonance, the diffraction intensity at the F-reflection exhibits a dip, whereas that at the S1-reflection exhibits a relatively large peak, as shown in Figs. 12(a) and (b), respectively. The size of the resonance feature (dip or peak) for the two reflections has been quantified by taking the ratio of diffraction intensities on and off the edge [arrows in Figs. 12(a) and (b)], following a previous study of a single composition, polycrystalline sample.[55] The respective results are shown in Figs. 12(c) and (d). The scaled intensity for the F-reflection shows no composition dependence above noise, having an average value (standard deviation) of 0.90(2). In contrast, the behavior for the S1-reflection exhibits a distinct peak at 30 at. % Ge [Fig. 12(d)]. Specifically, at 50 at. % Ge, the S1 resonance feature is ~40% above the background (diffraction intensity at 7.67 keV), and it increases to ~100% above the background near the Heusler stoichiometry with the hot spot Ge-enriched by 5 at. %.

The Co resonance features arise from the smaller Co form factor at the absorption-edge. When the form factor is summed with those from the other atoms, as in the case for the F-reflection, the total diffraction intensity is lowered at the edge [Fig. 12(a)]. The degree to which the intensity is lowered (size of the dip) is related to the atomic percent of Co in the lattice. In contrast, the diffraction intensity for the S1-reflection arises from a difference between the Co-sublattice (C-sites) and the others (A- and B-sites, see Table I). Therefore, when the Co scattering is reduced at resonance, this difference is enhanced and so is the diffracted intensity [Fig. 12(b)]. Correspondingly, the degree to which the intensity is enhanced at the Co-edge (size of the peak) is related to the Co-occupancy in its sublattice minus the Co-occupancy in the other sublattices (i.e. elemental swapping or antisites).

The composition-independent Co-resonance feature for the F-reflection is in stark contrast to the off-resonance counterpart with its distinctive narrow-ridge of high diffraction intensities [Fig. 11(a)]. This is expected since the reflection is completely insensitive to chemical ordering, though very sensitive to structural ordering. For the S1-reflection, on the other hand, the maximum Co-resonance feature [Fig. 12(d)] indicates the composition at which Co atoms are best ordered into the correct Co-sublattice (C-sites). When the resonance feature is diminished away from the hot spot, this may indicate that some Co atoms are missing in the C-sites (either vacancies or substituted by other atoms) and/or some of them occupy the other sites. Again, the composition-dependence of the resonance feature is very different from the off-resonance counterpart [Fig. 11(b)]. While the latter is convoluted by structural ordering, as mentioned above, the resonance intensity, particularly its ratio to the off-resonance counterpart, is only sensitive to the Co-occupancy within a structurally ordered unit cell and thus a useful qualitative measure of this type of disorders, though without resolving the specific disorders.

We now examine the behavior for the S2-reflection at the Co-edge, following the approach used in a previous anomalous XRD study to probe a specific type of chemical disorder, Co occupying the Mn B-site or B-antisites.[31] After the XRF background subtraction (II.C.), the measured intensities through the Co-resonance were fit using four adjustable parameters: (1) the amount of B-antisites, (2) the film thickness (level of self-absorption), and (3) a linear (two parameters) energy-dependent function for extrinsic instrumental effects [$I_0(E)$ in Eq. (3)]. In addition to the fit, various levels of B-antisites and A-antisites (Co occupying the Ge A-site) were also modeled. The results for $(Co_{2/3}Mn_{1/3})_{0.7}Ge_{0.3}$ are shown in Fig. 13. The fit (green trace) yields an occupation value of 3.5 ± 0.3% and a film thickness of 344 ± 21 Å. The thickness agrees with the value determined by XRF spectroscopy analysis discussed above (II.A). The model traces (red and blue), particularly the systematic change of their shapes, clearly show the high sensitivity of such a measurement to the specific anitsites. However, the amount of A-antisites (not considered previously),[31] when included in the fit as the fifth adjustable parameter, exhibits high correlations (> 0.99) with that of B-antisites. The correlation arises from the energy-dependence of the S2 structure factor (Table I). For instance, a correlated change in the amounts of Co in A and B sites will not affect the intensity. In other words, analyzing intensities at this edge and reflection alone cannot quantify the amounts of the two disorders. Therefore, this analysis is only sensitive to the *relative* amounts of the two disorders.

Various results presented above suggest the presence of C-site vacancies, particularly those associated with excess Ge. In order to explore the effect of these, S1-reflection at the Ge absorption-edge has been examined. The diffraction intensities and analysis for various Ge concentrations (from 27 to 48 at. %) at Co:Mn = 2 are shown in Fig. 14. As Ge concentration increases from the Heusler stoichiometry, the energy-dependent intensities change from a peak at

the Ge-edge of 11.103 keV with discernable fine-structures above the edge, to a valley centered just below the edge at 11.100 keV. By including vacancies at the C-site, a similar 4-parameter function to the one discussed above was used to fit the S1-intensity [black lines in Fig. 14(a)]. The resulting values for the vacancy exhibit an increasing trend versus Ge concentration [Fig. 14(b)]. While the same trend is reproduced in the MEAD analysis discussed below, this analysis at one absorption-edge still cannot avoid correlation problems with other potential disorders similar to the ones discussed above.

The above results clearly demonstrate that anomalous XRD is very sensitive to the various chemical disorders and can be used to deconvolute chemical ordering from the structural counterpart. Analysis of a single reflection at one absorption-edge can provide qualitative trend of a certain chemical disorder. However, this approach is unable to distinguish disorders that are correlated, such as site-swapping and anitsites. In the next section, we show that the correlation effects can be removed when multiple edges and reflections are measured and analyzed, so that all the chemical disorders present in a given alloy can be resolved and quantified.

2. Multiple-edge anomalous diffraction (MEAD)

Our MEAD experiments were performed at the compositions, where the highest degree of cubic structural ordering (hot spots) was revealed in the various XRD results discussed above. The measurements and analysis followed the procedures detailed in Sec. II.C, and the results for $(Co_{2/3}Mn_{1/3})_{1-x}Ge_x$ at 4 Ge concentrations (x = 30, 35, 40, 45 at. %), > 800 data points per spectrum, are shown in Fig. 15. Owing to the low diffraction intensity, the Heusler stoichiometry (x = 25 at. %) was not included in the study. The measured intensity statistics and energy intervals were chosen for simultaneous acquisition of diffraction intensity, and signals

from the near-edge-fine-structure and EXAFS, detected in the fluorescence mode. The fine-structures were used for solid-state corrections discussed in Sec. III.C.3 below.

The measured intensity ratios shown in Fig. 15 exhibit systematic changes versus Ge concentration. The level and shape of the measurements, including the fine-structure and near-edge features are all well reproduced by the analysis. The measured Ge-edge features for the film exhibit a + 6 eV shift in energy from the corresponding calculated edge for the Ge atoms (11.103 keV) that was confirmed by the beamline energy calibration using a bare Ge substrate. The shift in the near-edge structure evidently arises from the particular valency of the Ge atoms in this alloy, i.e. the chemical bonds between Ge and the neighboring atoms with the binding energy different from that of a native bulk Ge crystal. This effect is similar to the shift in binding energy due to oxidation or partial oxidation, i.e. modification of the chemical state, where the chemical bonds are to the neighboring oxygen atoms. As a result, the atomic form factors used for the model fits were shifted to line up with the measured Ge-edge of the film. In some cases, not all edges and reflections were measured, e.g. at 35 and 45 at. % Ge, but a unique fit was still attainable. The numerical results from each best fit are presented in Table IV. Our analysis shows that Co-Mn site swapping is absent in all compositions studied, so are Co-Ge swapping, and A- and B-site (the two lowest) vacancies. The Mn-Ge counterpart is the most prevalent, which is followed by Ge antisites and C-site vacancies.

From the MEAD analysis, the three most prevalent types of lattice site-specific chemical disorders at the various Ge concentrations are shown Fig. 16, whereas the corresponding site-occupancies of each element are shown in Supplemental Material Fig. S2 []. The large amount of Mn-Ge site swapping appears to be nearly independent of Ge concentration, while Ge-antisites and C-site vacancies all generally exhibit an increasing trend with Ge content. The

former [Fig. 16(a)] is most likely related to (anti-correlated with) the two hot spots for the diffraction intensity at the S2-reflection [Fig. 11(c)], but lacks the composition resolution to resolve the local hot spots near 30 and 40 at. % Ge. The trend in C-site vacancies [Fig. 16(b)] agrees with that from the single-edge analysis [Fig. 14(b)]. The single-edge, single-reflection fits, however, produce a higher level of vacancies, particularly at higher Ge concentrations, but since they are based on the single defect model, they are expected to over count, owing to the presence of other disorders, and thus less reliable than the multi-edge analysis. The amounts of Ge antisites [Fig. 16(c)] also increase with Ge concentration, and exhibit a more than two-fold preference for the B-site over the C-site, although the actual number of each antisites may be comparable, since there are twice as many C-sites as B-sites (Fig. 2). Also shown in Fig. 16 are the normalized χ^2 values from the corresponding least-square fits. The relatively high χ^2 values (> 3) appear to originate primarily from the high fluctuations at the absorption-edges, such that by removing some data points near the edge (≤ 10 eV), the χ^2 values can be reduced (< 3) [Fig. 16(d)].

We note that the uniqueness and effectiveness of the MEAD analysis were systematically tested, as described in Sec. I of Supplemental Material []. Overall, these considerations point to a robust and highly quantitative determination of identifiable site disorders using the analysis. If the resolution function and Debye-Waller disorder can be measured and modeled more precisely, the precision of this method can be further enhanced for detecting and quantifying amounts of the disorders $<< 1\%$.

The observed copious amount of Mn-Ge swapping and the absence of Mn-Co swapping are both inconsistent with the theoretical work based on the formation energy of this alloy system, which predicts the opposite.[18] At Co:Mn atomic ratio of 2, the Co-sites are the best

ordered (negligible swapping with either Mn or Ge), except for small amounts of vacancies. However, our study does indicate that off this atomic ratio, Co-occupancy related disorders are significantly enhanced, as indicated by the on- and off-resonance XRD features at S1-reflection [Figs. 11(b) and 12(d)]. This finding is consistent with previous experimental detection of Co-Mn swapping, which has been attributed to excess Co (Co:Mn > 2) occupying Mn sites.[31] In the case of Mn-Ge swapping, it not only has been detected experimentally,[19] but also is known to be prevalent off the Heusler stoichiometry.[56] Randomizing only the Mn and Ge sublattices would lead to the B2 (CsCl) structure,[56] where the A and B sites are no longer chemically distinct. The presence of the less ordered B2 structure and the transition to the more ordered $L2_1$ structure for this alloy system have been studied under various conditions, including strain and thermal annealing.[56, 57] The B2 is the high temperature thermodynamic structure for this alloy, and the transition to the low temperature $L2_1$ structure would be suppressed away from the Heusler stoichiometry.[58] Our low-temperature non-equilibrium epitaxial growth in the presence of tetragonal strain is expected to alter this transition and thus the nature of the room temperature structure.

In the [111] direction, the $L2_1$ structure is a superlattice with a quad-layer of Ge-Co-Mn-Co (ACBC) atomic layers, such that each Ge (Mn) layer is sandwiched between two Co layers, and thus separated from other layers of Mn (Ge). The B2 structure, on the other hand, is a bilayer superstructure along [111], where the A- and B-sites are occupied by random alloy of Mn-Ge, thus indistinguishable. The observed Mn-Ge swapping, when combined with the highly ordered Co layers, reveals several possible scenarios: "globally" random swapping of Mn-Ge between the A and B layers, a mixture of $L2_1$ and B2 structures, or a combination of the two. Whether the 30% Mn-Ge swapping is globally random in the film or there are separate B2 grains on the

order of 60% combined with ~40% $L2_1$ grains in the film would depend on the thermodynamics, but the two scenarios have not been distinguished in our analysis which only determined the structure corresponding to the ensemble average. It is not surprising that the presence of in-plane compressive strain can give rise to small in-plane domains and vacancies, consistent with the observed disorders. Conversely, reducing the strain is expected to promote transition to the more ordered $L2_1$ structure.[57] Furthermore, the observed preference of Ge anitistes in B-sites over C-sites is completely consistent with the preference for Mn-Ge swapping, especially at 30 at. % Ge, where there are significantly more Ge (not just the percentage) in B-sites.

The level of the disorders and their trends can also shed some light on the interplay between Ge concentration, thermodynamics, and epitaxial constraints. The rather constant amount of Mn-Ge swapping versus Ge concentration further supports the notion that the constant tetragonal strain (Figs. 9 and 10) plays a key role in giving rise to the disorder. It also suggests possible influence by the growth and annealing conditions, while the effect of lattice relaxation [Fig. 9(b)] may be negligible. However, the presence of highly ordered Co-sites suggests otherwise, that the film is sufficiently annealed, and thus the observed Mn-Ge swapping and the associated chemical domains are thermodynamically driven. In other words, the growth and annealing conditions, including our atomic layer sequential deposition (II.A), should promote the $L2_1$ structure but the presence of the tetragonal strain may have altered the energetics of the system. The fact that the off-resonance hot spots for S1- and S2-reflection shifted away from the Heusler stoichiometry (Figs. 11 and 12) further supports this interpretation.

Similarly, the presence of an in-plane compressive stress is expected to promote formation of vacancies, in addition to the smaller structural and chemical domains, but the origin for the observed preference for C-sites is unclear but likely to be energetic as well. The observed

increase in C-site vacancies with Ge concentration may suggest a gradual transition to the Zincblend (B3) or diamond structure, since half of the C-sites are equivalent to the body-interstitial sites in B3. However, the absence of B-site vacancies (equivalent to the edge-interstitials in B3 or diamond), combined with the relatively low values of C-site vacancies (~ 10 % at 50 at. % Ge) does not support this interpretation. Instead, there is no qualitative change in the site occupancies as Ge concentration increases (Fig. S2), which still correspond to a possible combination of $L2_1$ and B2 structures discussed above with preferential C-site vacancies.

The MEAD results clearly demonstrate the high resolution for the seven types of defects included in the analysis, to be at or below one percent of each site population (Table IV). Full understanding of these results would require knowledge of the local structures, including domain boundaries, stacking faults, and vacancies. One technique that is site-specific, sensitive to the local disorders is diffraction-anomalous-fine-structure (DAFS), especially when it is combined with the quantitative site occupancy information determined by MEAD. The results also provide the means for future opportunities to explore and ultimately control the $L2_1$-B2 transition in this alloy system by systematically change strain and growth and annealing conditions. Finally, band structure calculations [17, 18, 59] show that Mn-Ge swapping does not affect the halfmetallic state, as the Ge hybridized levels are well below the Fermi level, whereas disruption of the Co-sublattice does. Likewise, the presence of B2 structure is not expected to affect the magnetic properties. The [111] growth direction may, therefore, be ideal for suppressing the chemical defects that collapse the halfmetallic state in this material.

3. Near-edge effects

The measured near-edge-fine-structures at the Co- and Mn-edges were included in the respective anomalous form factors for the MEAD analysis. Inclusion of these solid-state corrections did improve the confidence in the analysis and to some extent the precision (reducing the χ^2 values of the fit), but these corrections were shown to be unimportant for extracting the prevalent chemical disorders. In particular, fits using only bare atom scattering factors and ignoring intensities near the edge produced quantitative values for the disorders in good agreement with those that included the solid-state effects.

The near-edge features at the Ge-edge could not be obtained from the non-grazing incidence EXAFS experiments, since the film was grown on Ge substrate. As mentioned above for XRF, grazing incidence experiments would lose composition sensitivity for ternary combinatorial samples. Instead, *ab-initio* calculations (based on the FEFF8 software package [42]) were used to model the photoelectron scattering from a Ge absorber in the Heusler structure and calculate the Ge atomic form factor near the absorption-edge. Photoelectrons below approximately 20 eV have no inelastic excitations available in the free electron gas, being below the plasmon energy. Therefore, their mean-free-path becomes very long in the crystal and can scatter coherently from distant neighboring atoms and thus become sensitive to the types of disorders around Ge.

Two sets of analysis at two compositions for anomalous intensities at the S1-reflection and Ge-edge are shown in Fig. 17. Without the solid-state corrections [Figs. 17(a) and (b)], the near-edge structures in the measured intensities are clearly not reproduced by the model fits, although the pre-edge and extended post-edge trends fare better. The scattering factors used in this calculation was obtained by using HEFAESTUS program with the bare atom absorption

factors in the FEFF8 software package.[41, 60] With the addition of the calculated solid-state corrections [Figs. 17(c) and (d)], there is improvement in the near-edge structures, but a large peak 10 eV above the edge exhibited in the calculations does not exist in the measurements. Further improvement to the calculated solid-state corrections involved inclusion of random 30% site-swapping between A and B sites (approximately the amount of Mn-Ge swapping obtained from the MEAD analysis discussed above), as shown in Figs. 17(e) and (f). Here, the calculations reproduce the measured intensities extremely well for both compositions even though differences still exist in the near-edge features. These calculated corrections were used in all MEAD analysis, including those for the Ge-edge at S1-reflection shown in Fig. 14. This result provides a powerful supporting evidence for the validity of the MEAD analysis. Further details on the effects of the extended-fine-structures in the analysis can be found in Sec. V of Supplemental Material [].

IV. SUMMARY

The effects of composition and epitaxial constraints on structural and chemical ordering in epitaxial films of $Co_xMn_yGe_z$ grown on Ge (111) substrates have been systematically investigated. A high-resolution ternary epitaxial phase diagram for this system has been obtained. A small number of structural phases have been stabilized over a large compositional range, including a potentially new hexagonal phase near the composition of $Co_2Mn_3Ge_6$, which is ferromagnetic at room temperature. The Ge Heusler alloy Co_2MnGe has been studied extensively, and its structural and chemical ordering is shown to be robust over a wide range of Ge compositions (20-50 at. % Ge) but extremley sensitive to the Co to Mn atomic ratio. This potentially explains the high levels of disorders reported in thin film samples that are typically off-stoichiometry. The film is coherent in-plane with a 60° rotation in its stacking along [111]

with respect to that of the substrate, while the ~1.5% lattice mismatch is accomodated by the out-of-plane tetragonal strain. Within the cubic ROI, the film's lattice obeys Vegard's law. The highest degree of ordering in the epitaxial film is determined to be off the Heusler stoichiometry at 30 at. % Ge and Co:Mn = 2.

Lattice site-specific chemical disorders in the epitaxial film, including site-swapping, antisites, and vacancies, and their dependence on alloy concentration have been probed and quantified for the first time by the use of multiple-edge anomalous diffraction experiments and analysis. Results from the MEAD analysis reveal high levels of Mn-Ge swapping (~26%), accompanied by moderate levels of Ge antisites and Co-site vacancies. The level of antisites and vacancies, and their dependence on Ge concentration have been attributed to excess Ge off-stoichiometry. Co-sites are found to be the most chemically ordered, exhibiting negligible swapping with either Mn- or Ge-sites. The presence of Mn-Ge swapping and absence of Co-Mn swapping both contradict first principles calculations. The observed Mn-Ge swapping is consistent with either a random swapping of Mn and Co or a mixture of $L2_1$ and B2 structures. The presence of a tetragonal distortion in the epitaxial film along the [111] direction appears to play an important role in controlling the energetics of the system, giving rise to the specific site-swapping, antisites, and vacancies. These findings provide impetus to further explore the transition between $L2_1$ and B2 structures as a function of epitaxial contraints and synthesis conditions. A future challenge is to correlate these effects with spin-dependent electronic states that also need to be further investigated.

H. Acknowledgements

We thank S. Vogt at APS for assistance in XRF analysis, and E. Kravtsov at Institute of Metal Physics, Russian Academy of Sciences for exploring additional routes to obtain local structure information from the anomalous diffraction data. The work is supported by US DOE BES DE-FG02-05ER46216. Combinatorial synthesis instrumentation was supported by U.S. Department of Defense, Grant No. W911NF-05-1-0173. Use of the Advanced Photon Source is supported by the US Department of Energy, Office of Sciences, Office of Basic Energy Sciences, under contract no. DE-AC02-06CH11357. An APS subcontract no. 5F-00428 for partial student support (BAC) is also acknowledged. Work at the National Synchrotron Light Source II, Brookhaven National Laboratory, was supported by the U.S. Department of Energy, Office of Science, Office of Basic Energy Sciences, under Contract No. DE-SC0012704.

References

1. F. Heusler, Verh. Dtsch. Phys. Ges. **5** (12), 219 (1903).

2. P. J. Webster, J Phys Chem Solids **32** (6), 1221-1231 (1971).

3. R. A. de Groot, F. M. Mueller, P. G. van Engen and K. H. J. Buschow, Phys. Rev. Lett. **50** (25), 2024-2027 (1983).

4. S. Ishida, T. Masaki, S. Fujii and S. Asano, Physica B: Condensed Matter **245** (1), 1-8 (1998).

5. S. Ishida, S. Fujii, H. Nagayoshi and S. Asano, Physica B: Condensed Matter **254** (3-4), 157-165 (1998).

6. S. Picozzi, A. Continenza and A. Freeman, Physical Review B **66** (9), 094421 (2002).

7. W. E. Pickett and J. S. Moodera, Phys. Today **54** (5), 39-44 (2001).

8. T. Ambrose, J. J. Krebs and G. A. Prinz, Applied Physics Letters **76** (22), 3280 (2000).

9. M. P. Raphael, B. Ravel, M. A. Willard, S. F. Cheng, B. N. Das, R. M. Stroud, K. M. Bussmann, J. H. Claassen and V. G. Harris, Applied Physics Letters **79** (26), 4396 (2001).

10. B. Ravel, M. Raphael, V. Harris and Q. Huang, Physical Review B **65** (18), 184431 (2002).

11. A. Rajanikanth, Y. K. Takahashi and K. Hono, J Appl Phys **101** (2), 023901 (2007).

12. M. Yamamoto, T. Marukame, T. Ishikawa, K. Matsuda, T. Uemura and M. Arita, J. Phys. D-Appl. Phys. **39** (5), 824-833 (2006).

13. T. Ishikawa, T. Marukame, K.-i. Matsuda, T. Uemura, M. Arita and M. Yamamoto, J Appl Phys **99** (8), 08J110 (2006).

14. S. Tsunegi, Y. Sakuraba, M. Oogane, K. Takanashi and Y. Ando, Applied Physics Letters **93** (11), 112506 (2008).

15. M. Jourdan, J. Minár, J. Braun, A. Kronenberg, S. Chadov, B. Balke, A. Gloskovskii, M. Kolbe, H. J. Elmers, G. Schönhense, H. Ebert, C. Felser and M. Kläui, Nat Commun **5** (2014).

16. L. Ritchie, G. Xiao, Y. Ji, T. Chen, C. Chien, M. Zhang, J. Chen, Z. Liu, G. Wu and X. Zhang, Physical Review B **68** (10), 104430 (2003).

17. I. Galanakis, P. Dederichs and N. Papanikolaou, Physical Review B **66** (17), 174429 (2002).

18. S. Picozzi, A. Continenza and A. J. Freeman, Physical Review B **69** (9), 094423 (2004).

19. P. J. Brown, K. U. Neumann, P. J. Webster and K. R. A. Ziebeck, J. Phys.-Condes. Matter **12** (8), 1827-1835 (2000).

20. M. P. Raphael, B. Ravel, Q. Huang, M. A. Willard, S. F. Cheng, B. N. Das, R. M. Stroud, K. M. Bussmann, J. H. Claassen and V. G. Harris, Phys. Rev. B **66** (10), 104429 (2002).

21. F. Tsui and L. He, Rev Sci Instrum **76** (6), 062206 (2005).

22. Y. K. Yoo and F. Tsui, Mrs Bull **27** (4), 316-323 (2002).

23. Y. S. Chu, A. Tkachuk, S. Vogt, P. Ilinski, D. A. Walko, D. C. Mancini, E. M. Dufresne, L. He and F. Tsui, Appl Surf Sci **223** (1-3), 175-182 (2004).

24. Y. Zhong, Y. S. Chu, B. A. Collins and F. Tsui, Appl Surf Sci **254** (3), 714-719 (2007).

25. S. Vogt, Y. S. Chu, A. Tkachuk, P. Ilinski, D. A. Walko and F. Tsui, Appl Surf Sci **223** (1-3), 214-219 (2004).

26. B. A. Collins, Ph.D. thesis, University of North Carolina at Chapel Hill, 2009.

27. F. Tsui, L. He, A. Tkachuk, S. Vogt and Y. Chu, Physical Review B **69** (8), 081304 (2004).

28. L. He, B. A. Collins, F. Tsui, Y. Zhong, S. Vogt and Y. S. Chu, Journal of Vacuum Science & Technology B: Microelectronics and Nanometer Structures **25** (4), 1217 (2007).

29. B. Collins, Y. Chu, L. He, Y. Zhong and F. Tsui, Physical Review B **77** (19), 193301 (2008).

30. L. He, B. A. Collins, F. Tsui and Y. S. Chu, Journal of Vacuum Science & Technology B: Microelectronics and Nanometer Structures **29** (3), 03C124 (2011).

31. B. Ravel, J. O. Cross, M. P. Raphael, V. G. Harris, R. Ramesh and V. Saraf, Applied Physics Letters **81** (15), 2812 (2002).

32. B. A. Collins, Y. C. Zhong, Y. S. Chu, L. He and F. Tsui, J Vac Sci Technol B **25** (3), 999-1003 (2007).

33. F. Tsui, L. He, D. Lorang, A. Fuller, Y. S. Chu, A. Tkachuk and S. Vogt, Appl Surf Sci **252** (7), 2512-2517 (2006).

34. F. Tsui, L. He and L. Ma, in *Combinatorial and Artificial Intelligence Methods in Materials Science*, edited by I. Takeuchi, J. M. Newsam, L. T. Wille, H. Koinuma and E. J. Amis (Materials Research Society, Warrendale, 2002), Vol. 700, pp. 39-44.

35. I. K. Robinson and D. J. Tweet, Rep. Prog. Phys. **55** (5), 599-651 (1992).

36. S. Vogt, Journal De Physique Iv **104**, 635-638 (2003).

37. S. Vogt, http://www.stefan.vogt.net/downloads.html (2008).

38. P. K. Muduli, W. C. Rice, L. He, B. A. Collins, Y. S. Chu and F. Tsui, J. Phys.-Condes. Matter **21** (29), 296005-296011 (2009).

39. P. K. Muduli, W. C. Rice, L. He and F. Tsui, J Magn Magn Mater **320** (23), L141-L143 (2008).

40. Y. S. Chu, I. K. Robinson and A. A. Gewirth, Physical Review B **55** (12), 7945-7954 (1997).

41. D. T. Cromer and D. Liberman, Journal of Chemical Physics **53** (5), 1891-1898 (1970).

42. J. J. Rehr, J. Mustre de Leon, S. I. Zabinsky and R. C. Albers, Journal of the American Chemical Society **113** (14), 5135-5140 (1991).

43. P. Villars, H. Okamoto and A. Prince, *Handbook of Ternary Alloy Phase Diagrams*. (ASM International, Materials Park, OH, 1995).

44. A. SzytuŁa, A. T. P□dziwiatr, Z. Tomkowicz and W. Bażela, J Magn Magn Mater **25** (2), 176-186 (1981).

45. V. Johnson, Inorganic Chemistry **14** (5), 1117-1120 (1975).

46. M. Ellner, Journal of Applied Crystallography **13** (Feb), 99-100 (1980).

47. H. Baker, *ASM Handbook: Alloy Phase Diagrams*. (ASM International, 1992).

48. *The Powder Diffraction File*. (International Centre for Diffraction Data, 2006).

49. G. A. Prinz, Physical Review Letters **54** (10), 1051-1054 (1985).

50. R. Walmsley, J. Thompson, D. Friedman, R. M. White and T. H. Geballe, Magnetics, IEEE Transactions on **19** (5), 1992-1994 (1983).

51. P. M. Marcus and V. L. Moruzzi, Solid State Commun. **55** (11), 971-975 (1985).

52. R. J. Weiss and K. J. Tauer, J Phys Chem Solids **4** (1–2), 135-143 (1958).

53. B. Heinrich, A. S. Arrott, J. F. Cochran, C. Liu and K. Myrtle, Journal of Vacuum Science & Technology A **4** (3), 1376-1379 (1986).

54. G. Fuster, N. E. Brener, J. Callaway, J. L. Fry, Y. Z. Zhao and D. A. Papaconstantopoulos, Physical Review B **38** (1), 423-432 (1988).

55. S. Ouardi, G. H. Fecher, B. Balke, A. Beleanu, X. Kozina, G. Stryganyuk, C. Felser, W. Klöß, H. Schrader, F. Bernardi, J. Morais, E. Ikenaga, Y. Yamashita, S. Ueda and K. Kobayashi, Physical Review B **84** (15), 155122 (2011).

56. M. Kogachi, T. Fujiwara and S. Kikuchi, J. Alloy. Compd. **475** (1-2), 723-729 (2009).

57. H. T. Nembach, T. J. Silva, J. M. Shaw, M. L. Schneider, M. J. Carey, S. Maat and J. R. Childress, Physical Review B **84** (5), 054424 (2011).

58. M. Kogachi, N. Tadachi and T. Nakanishi, Intermetallics **14** (7), 742-749 (2006).

59. K. O□zdog□an and I. Galanakis, J Appl Phys **110** (7), 076101 (2011).

60. B. Ravel and M. Newville, J Synchrotron Radiat **12** (Pt 4), 537-541 (2005).

Figure Captions

FIG. 1. (Color online) (a) Schematic diagram (plan-view) of the $Co_xMn_yGe_z$ sample and the various regions of interest (ROI) on a Ge (111) substrate (the black outline), and (b) correspondingly in the same orientation as in (a), the crystallographic directions of the substrate in cubic indices with the surface normal [111] out-of-the-page. The ternary region with the measured compositional grid is indicated by the triangle (green dashed lines). The blue trapezoid and the red rectangle are the two ROI studied. The regions of the trapezoid outside the triangle correspond to those of binary alloys (Mn_xGe_{1-x} and Co_xGe_{1-x}). The black dash-dotted line and the circle indicate the respective positions for Co:Mn = 2 and Co_2MnGe.

FIG. 2. (Color online) Schematic diffraction patterns for $Co_xMn_yGe_z$ grown epitaxially on Ge (111) represented in the hexagonal coordinate system. Key reflections are labeled by their hexagonal and cubic coordinates. The box indicates the typical range of short *L*-scans described in the text.

FIG. 3. (Color online) Schematic diagram of the Heusler structure that consists 3 unique sites each filled with one element: A-site with 4 Ge atoms, B-site with 4 Mn atoms, and C-site with 8 Co atoms.

FIG. 4. (Color online) Scaling of multiple-edge anomalous diffraction intensities at three unique reflections in the Ge Heusler alloy. (a) Integrated intensities (normalized to incoming flux via an ion chamber detector) from out-of-plane *L*-scans for $(Co_{2/3}Mn_{1/3})_{1-x}Ge_x$ at four compositions (*x* values) used to scale the energy-scans. (b) Scaled and assembled diffraction intensities for $(Co_{2/3}Mn_{1/3})_{0.7}Ge_{0.3}$.

FIG. 5. (Color online) Composition-dependent XRD patterns along compositional line of $(Co_xMn_{1-x})_{0.75}Ge_{0.25}$. (a) Image of log diffraction intensity through $(01L)_h$ (color scale on the right) versus L-position in reciprocal lattice units (rlu) and concentration. The right axis is calculated for cubic structure. (b) Integrated peak intensity, and (c) its FWHM from Voigt fits versus concentration.

FIG. 6. (Color online) Composition-dependent XRD patterns along compositional line of $Co_{0.5x}Mn_{0.5x}Ge_{1-x}$. (a) Image of log diffraction intensity through $(01L)_h$ (color scale on the right) versus L-position and concentration. Out of plane lattice parameter of the film on the right axis is calculated for hexagonal structure. (b) Integrated peak intensity and (c) its FWHM from Voigt fits. Dashed lines represent phase boundaries, and the arrows indicate the composition of CoMnGe.

FIG. 7. (Color online) XRD peak through $(01L)_h$ versus composition: (a) L-position of the diffraction peak, and (b) log integrated intensity and (c) FWHM of the peak. When multiple peaks are present, the parameters for the peak with the highest integrated intensity are shown. Measurements outside of the ternary region correspond to results for binary alloys of Mn_xGe_{1-x} (left) and Co_xGe_{1-x} (right). The composition grid was determined experimentally. Dash-dotted lines highlights the Co:Mn ratios of 2 and 4, whereas the dashed lines correspond to other Co:Mn ratios, as indicated in (c).

FIG. 8. (Color online) Ternary phase diagrams of $Co_xMn_yGe_z$. (a) Structural phase diagram: single and multiple phase regions are indicated by solid and striped colors, respectively.

Continuous and discontinuous phase boundaries are indicated by dashed and solid lines, respectively. (b) Magnetic phase diagram: contours of ferromagnetic regions at various temperatures and grey scale image of MOKE intensity at 300 K in the zero-field remanent state that corresponds remanent magnetization. The contours at 400 and 450 K (not shown) are identical to that of 470 K within experimental uncertainties. The dash-dotted and dashed lines correspond to Co:Mn ratios of 2:1, 1:1, and 3:4, respectively. The composition grid was determined experimentally. Circles indicate the compositions of several known compounds discussed in the text.

FIG. 9. (Color online) Out-of-plane and in-plane lattice parameters versus composition. (a) Values of $(c'-c)/c$ from *L*-scan of the $(014)_h$ reflection, and (b) $(a'-a)/a$ from *K*-scan across the $(102)_h$ reflection. The color scale has been discretized for clarity and the white contour lines correspond to zero mismatch with the substrate. Black lines correspond to measured composition grid. The ROI for the two reflections are slightly different.

FIG. 10. (Color online) Lattice constant and strain state of the film versus composition: (a) lattice constant a_0' and lattice mismatch ε_0 with the Ge substrate and (b) in-plane strain $\varepsilon_{\|}$. The blue-red boundary in (a) corresponds to the bulk lattice constant of Co_2MnGe. White contour lines (top right) indicate the location of lattice matching with Ge. Color contours are discretized for clarity. Black lines correspond to measured composition grid.

FIG. 11. (Color online) Composition dependence of integrated diffraction intensities at various reflections: (a) $(014)_h$, (b) $(102)_h$, and (c) $(011)_h$. (d) Log integrated intensity ratio between the

S1-reflection $(102)_h$ and its twin $(012)_h$. Below the red dotted line, the diffraction intensity from the twin $(012)_h$ could not be detected above the background, so the intensity ratio is between the S1-reflection and the background instead. White lines correspond to measured composition grid. The ROI for the different reflections are slightly different from each other.

FIG. 12. (Color online) Composition dependence of anomalous diffraction intensities at the Co-edge. Diffracted intensity versus energy at various Ge concentrations and Co:Mn = 2 [i.e. $(Co_{2/3}Mn_{1/3})_{1-x}Ge_x$] for two reflections: (a) $(014)_h$ and (b) $(102)_h$. Arrows indicate the size of the resonant features. Ratios between intensities on- and off-resonance (7.71 and 7.67 keV, respectively) for the two reflections: (c) $(014)_h$ and (d) $(102)_h$. White lines correspond to measured composition grid.

FIG. 13. (Color online) Anomalous diffraction intensities of $(Co_{2/3}Mn_{1/3})_{0.7}Ge_{0.3}$ at the S2-reflection and around the Co-edge: measured intensity (circles) and different models of Co-antisites at various levels (lines). The green line is a model fit of the measurement with Co in the B-site at (3.5 ± 0.3)%. Statistical uncertainties, shown with a few data points, are on the order of the background noise.

FIG 14. (Color online) (a) Measured anomalous diffraction intensities around the Ge-edge at the S1-reflection (red) for various Ge concentrations at Co:Mn = 2. Model fits (black lines) with only C-site vacancies as an allowed disorder parameter. The spectra are shifted vertically for clarity. (b) C-site vacancies versus Ge concentration from the analysis. Uncertainty is comparable to the size of the circle.

FIG. 15. (Color online) Measured anomalous diffraction intensities versus energy (red points) and MEAD fits (black lines) for $(Co_{2/3}Mn_{1/3})_{1-y}Ge_y$ at various Ge concentrations: (a) 30, (b) 35, (c) 40, and (d) 45 at. %.

FIG. 16. (Color online) Populations of the most significant disorders from the MEAD analysis at several Ge-concentrations (Co:Mn = 2): (a) Mn-Ge site swapping, (b) C-site vacancies, and (c) Ge antisites as a percentage of site population. Uncertainties are comparable to the size of the points. (d) Normalized χ^2 values from the fits using all the measured points (close circles) and those with the near-edge data removed (open circles).

FIG. 17. (Color online) Comparison between measured anomalous diffraction intensities (at the S1-reflection and the Ge-edge) and several model fits for $(Co_{2/3}Mn_{1/3})_{1-x}Ge_x$ at two Ge concentrations: x = 27 (left column) and 48 at. % (right column). Lines correspond to fits with (a) and (b) only bare atom anomalous corrections (no solid-state corrections), (c) and (d) *ab-initio* solid-state corrections for the Heusler alloy, and (e) and (f) *ab-initio* solid-state corrections for the Heusler alloy with 30% Mn-Ge site-swapping.

TABLE I. Three unique Bragg reflections of the Heusler structure in both the cubic and the hexagonal indices, their abbreviations used in the text, and properties. The asterisks indicate the corresponding indices for the 60°-twin reflections.

Abbr.	Studied Reflection		Structure Factor	Bragg Condition
	Cubic index	Hexagonal index		
F	(022)*	(104)* = (014)	$f_A + f_B + 2f_C$	If $H + K + L = 2 \times$ even integers
S1	(002)*	(012)* = (102)	$f_A + f_B - 2f_C$	If $H + K + L = 2 \times$ odd integers
S2	$(\bar{1}11)$*	(101)* = (011)	$f_A - f_B$	If $H + K + L =$ odd integers

TABLE II. Occupancy parameters used in the analysis [Eq. (3)]. Subscripts A, B, and C correspond to the three respective unique sites in the unit cell of C_2BA structure (Fig. 2). Values are in site percentage, and thus a factor of 2 for the C-sites. The conversions are described in the text.

Type	Site	Elements	Conversion
Site-Swapping	A-B	Ge-Mn	$\min(M_A, G_B)$
	B-C	Mn-Co	$\min(C_B, 2 \cdot M_C)$
	C-A	Co-Ge	$\min(2 \cdot G_C, C_A)$
Vacancies	A	Ge	$100 - C_A - M_A - G_A$
	B	Mn	$100 - C_B - M_B - G_B$
	C	Co	$100 - C_C - M_C - G_C$
Ge Antisites	B	Mn	$G_B - M_A$
	C	Co	$G_C - C_A/2$

TABLE III. Vegard's law coefficients for the two compositional regions described in the text [Figs. 9(a) and 10(a)].

Ge concentration	a_{Co} (Å)	a_{Mn} (Å)	a_{Ge} (Å)
$z < 0.5$	5.49 ± 0.04	6.38 ± 0.09	5.68 ± 0.03
$z > 0.5$	5.6 ± 0.2	7.2 ± 0.2	5.5 ± 0.2

TABLE IV. Results of MEAD analysis for $(Co_{2/3}Mn_{1/3})_{1-x}Ge_x$ at four Ge concentrations (x). Values are in percent of each site with uncertainty of the last decimal(s) in parenthesis.

Disorder Type	30 at. % Ge	35 at. % Ge	40 at. % Ge	45 at. % Ge
σ	0.11(1)	0.21(1)	0.18(1)	0.23(1)
Mn-Ge Swapping	26.6(3)	34.0(3)	25.8(2)	25.8(3)
Co-Mn Swapping	0.0(6)	0.0(5)	0.0(5)	0.0(6)
Ge-Co Swapping	1.1(7)	0.0(5)	4.5(5)	0.0(8)
A-Site Vacancies	0.31(5)	0.30(3)	0.35(2)	0.6(2)
C-Site Vacancies	7.17(5)	6.98(3)	8.47(3)	9.55(10)
Ge Replacing Mn	10.4(1.0)	16.7(9)	27.6(8)	38.4(1.1)
Ge Replacing Co	2.8(1.0)	9.3(8)	12.9(8)	16.7(8)

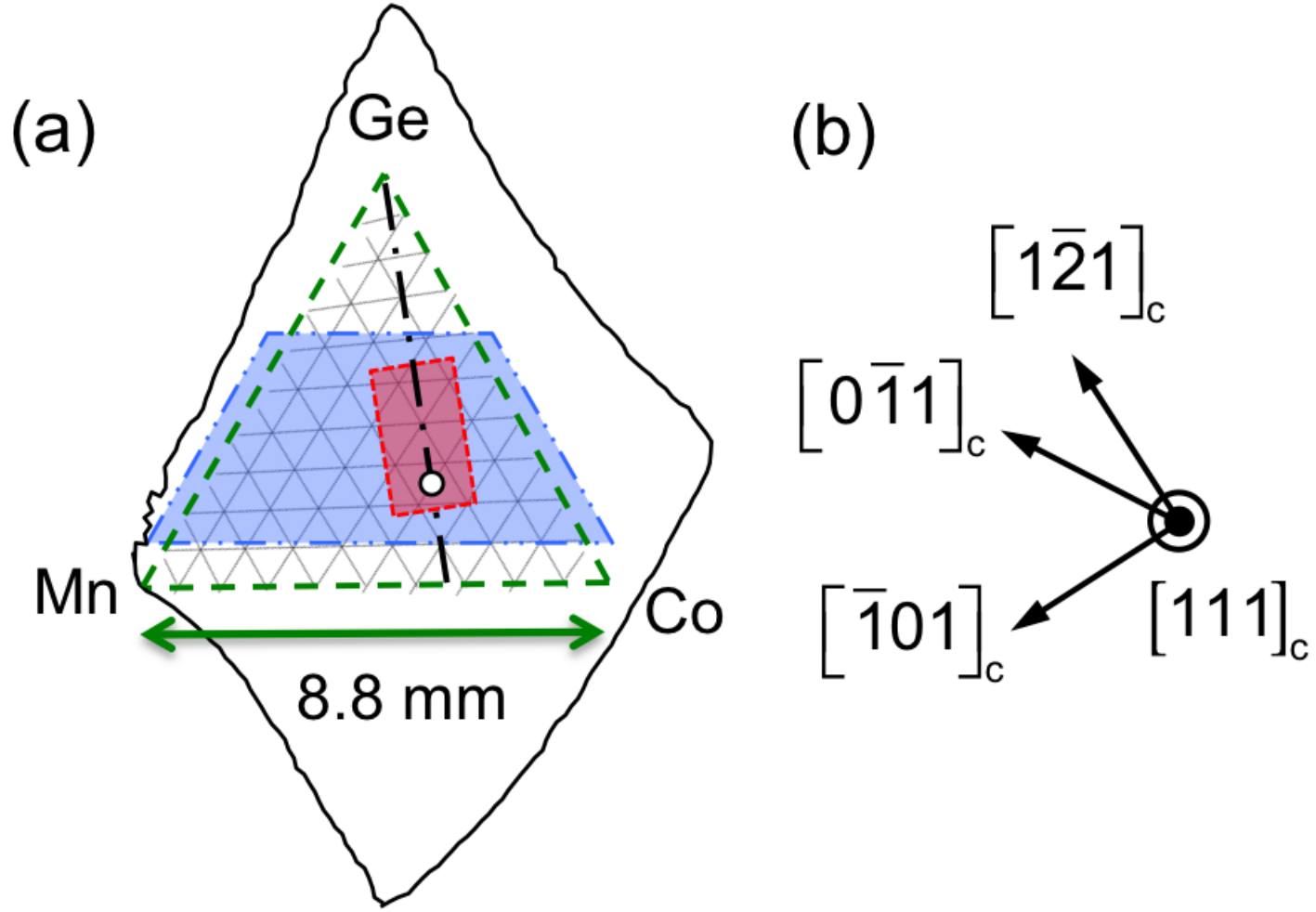
(a)
Ge
Mn
Co
8.8 mm
(b)
$[1\bar{2}1]_c$
$[0\bar{1}1]_c$
$[\bar{1}01]_c$
$[111]_c$

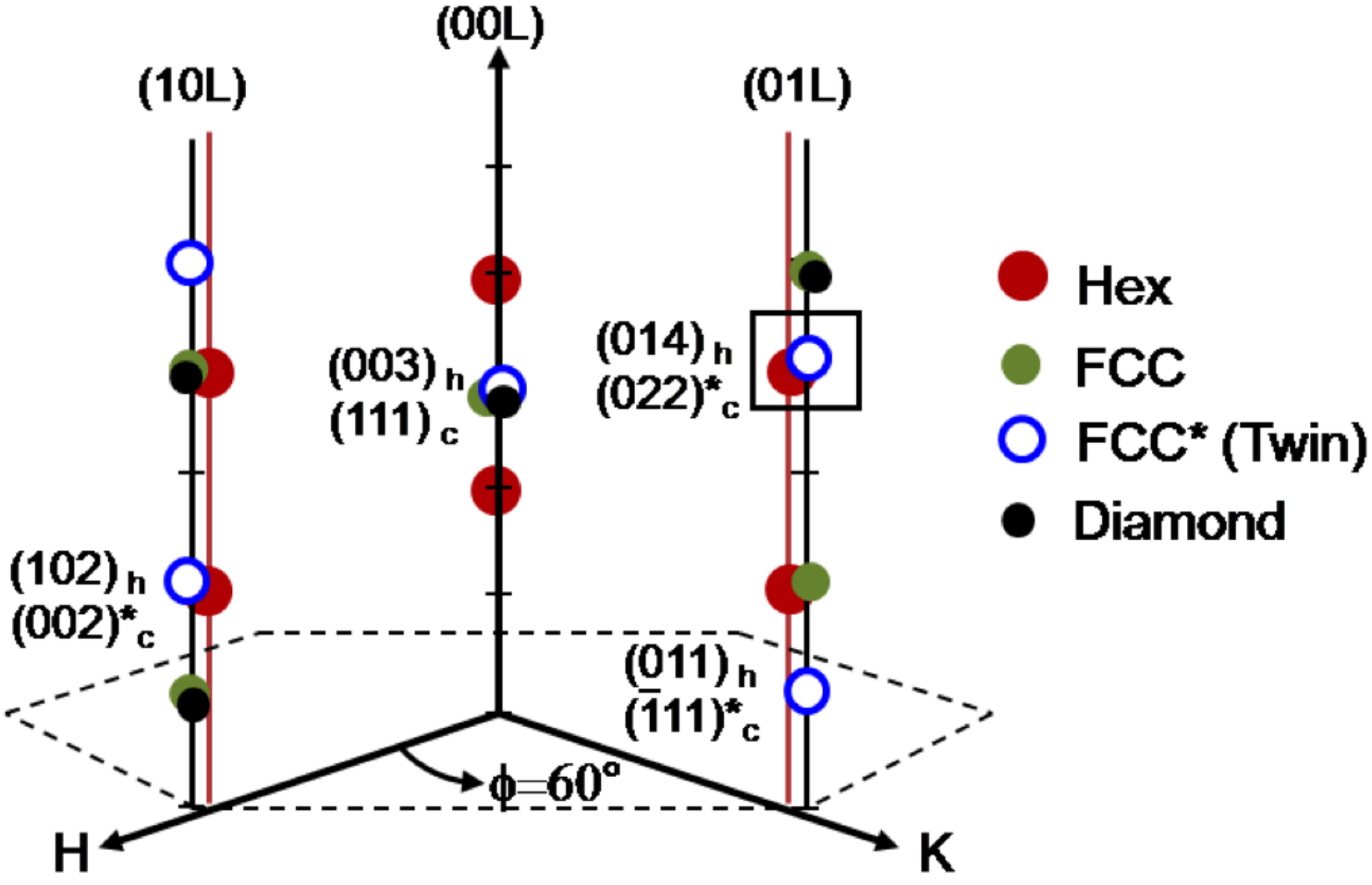
(00L)
(10L)
(01L)
(003) h
(111) c
(014) h
(022)*c
(102) h
(002)*c
(0̄11) h
(1̄11)*c
ϕ=60°
H
K
Hex
FCC
FCC* (Twin)
Diamond

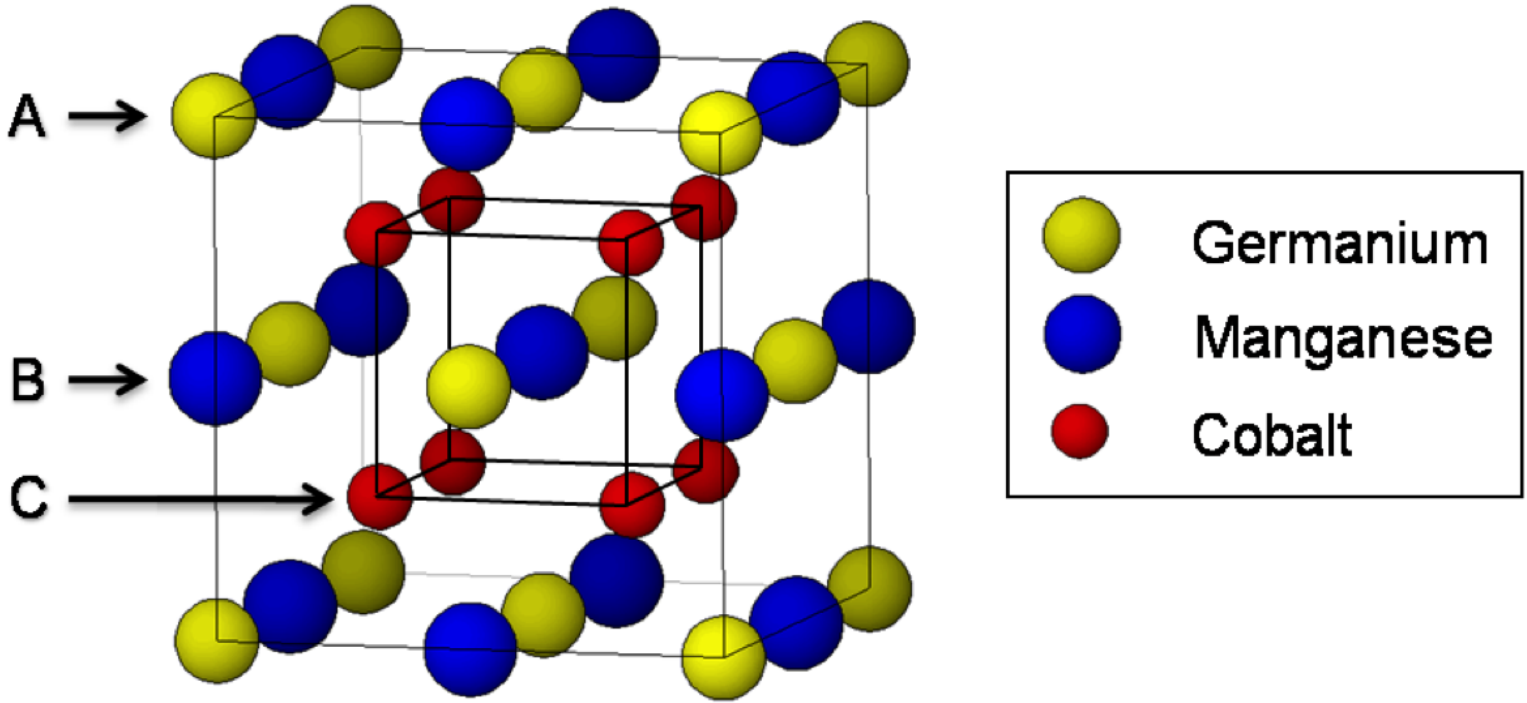
A
B
C
Germanium
Manganese
Cobalt

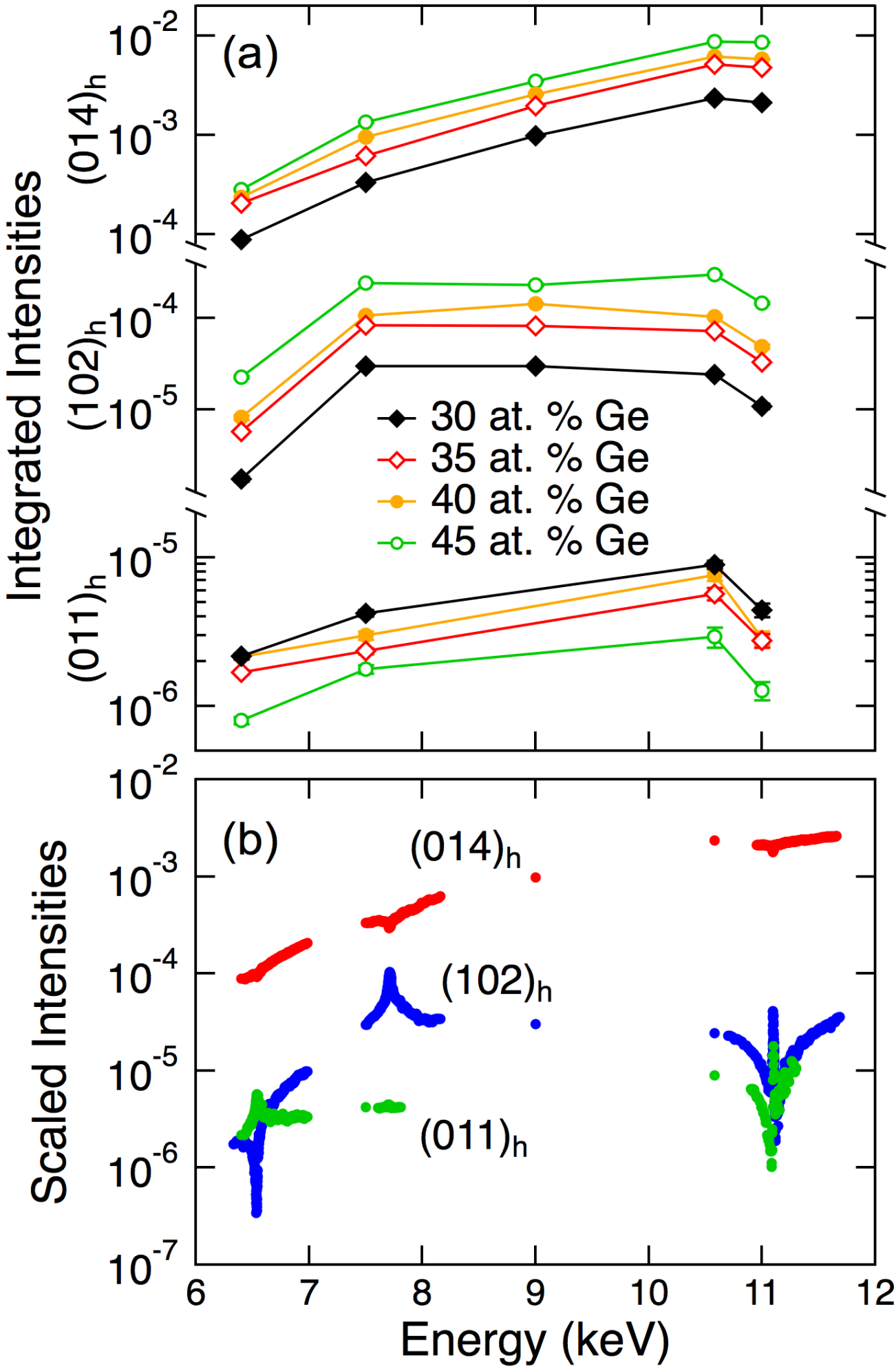
(a)
Integrated Intensities
(014)h
(102)h
(011)h
30 at. % Ge
35 at. % Ge
40 at. % Ge
45 at. % Ge
(b)
Scaled Intensities
(014)h
(102)h
(011)h
Energy (keV)

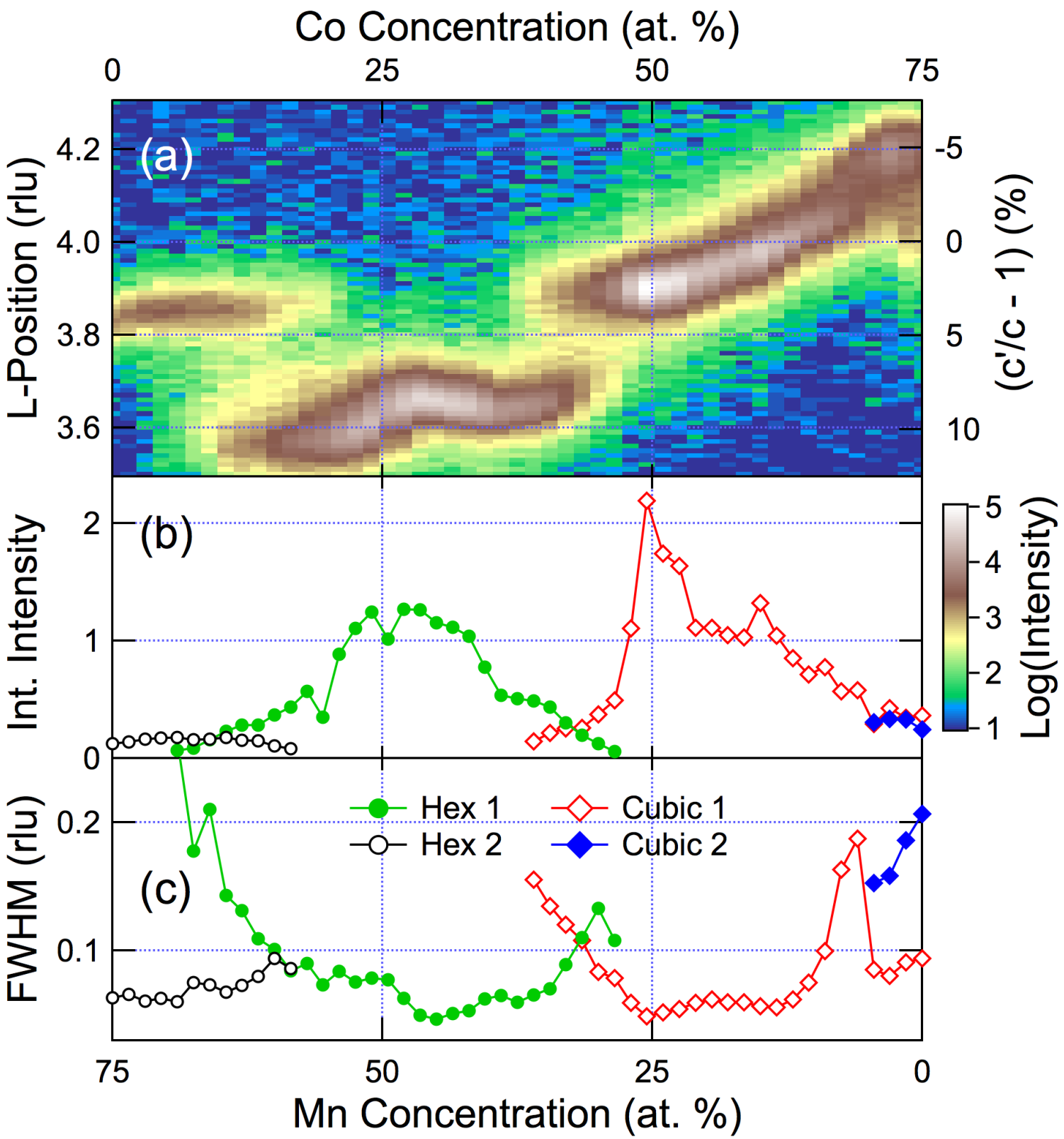
Co Concentration (at. %)
0
25
50
75
(a)
L-Position (rlu)
4.2
4.0
3.8
3.6
-5
0
5
10
(c'/c - 1) (%)
(b)
Int. Intensity
2
1
0
5
4
3
2
1
Log(Intensity)
(c)
FWHM (rlu)
0.2
0.1
Hex 1
Hex 2
Cubic 1
Cubic 2
75
50
25
0
Mn Concentration (at. %)

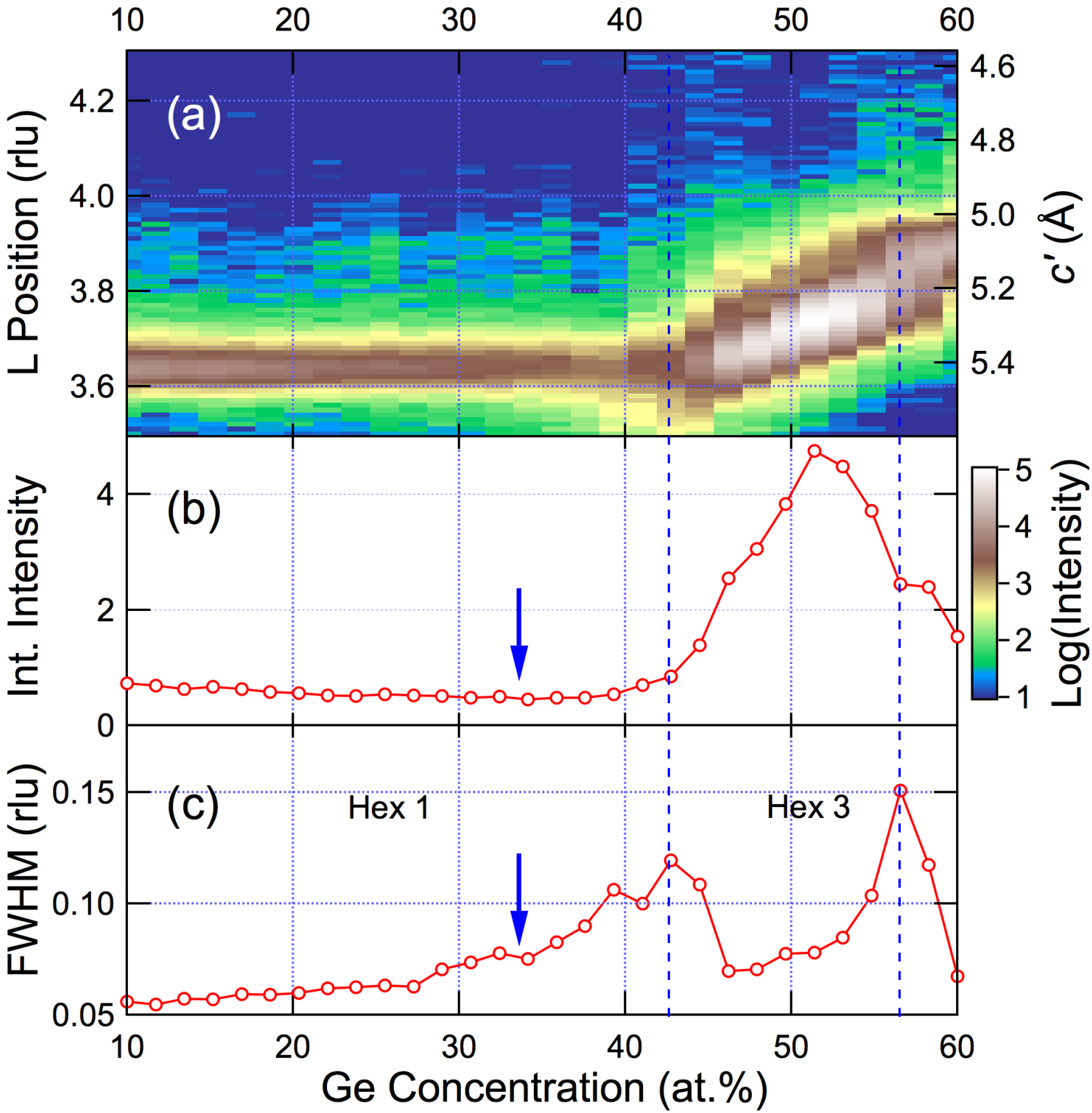
(a)
(b)
(c)
L Position (rlu)
c′ (Å)
Int. Intensity
Log(Intensity)
FWHM (rlu)
Hex 1
Hex 3
Ge Concentration (at.%)
10
20
30
40
50
60
4.2
4.0
3.8
3.6
4.6
4.8
5.0
5.2
5.4
4
2
0
5
4
3
2
1
0.15
0.10
0.05

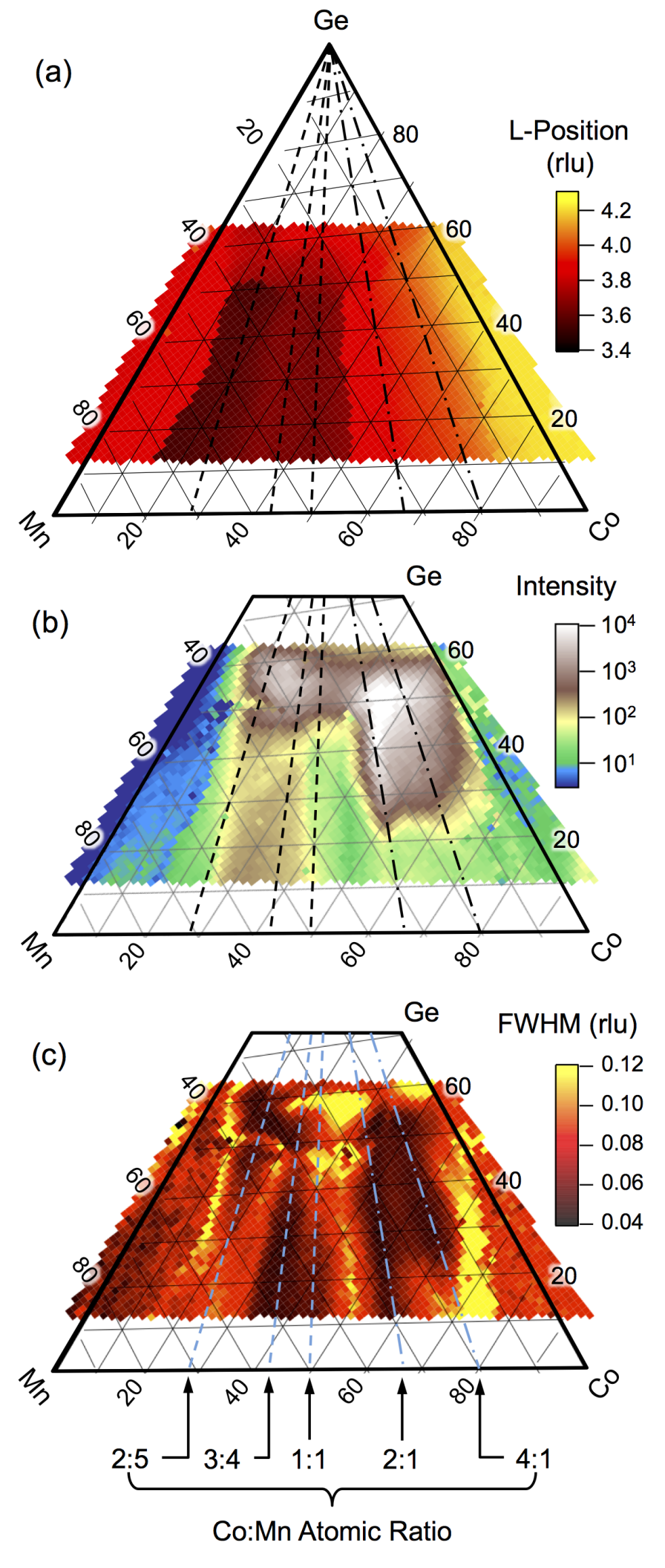
(a)
Ge
Mn
Co
20
40
60
80
L-Position
(rlu)
4.2
4.0
3.8
3.6
3.4
(b)
Intensity
10^4
10^3
10^2
10^1
(c)
FWHM (rlu)
0.12
0.10
0.08
0.06
0.04
2:5
3:4
1:1
2:1
4:1
Co:Mn Atomic Ratio

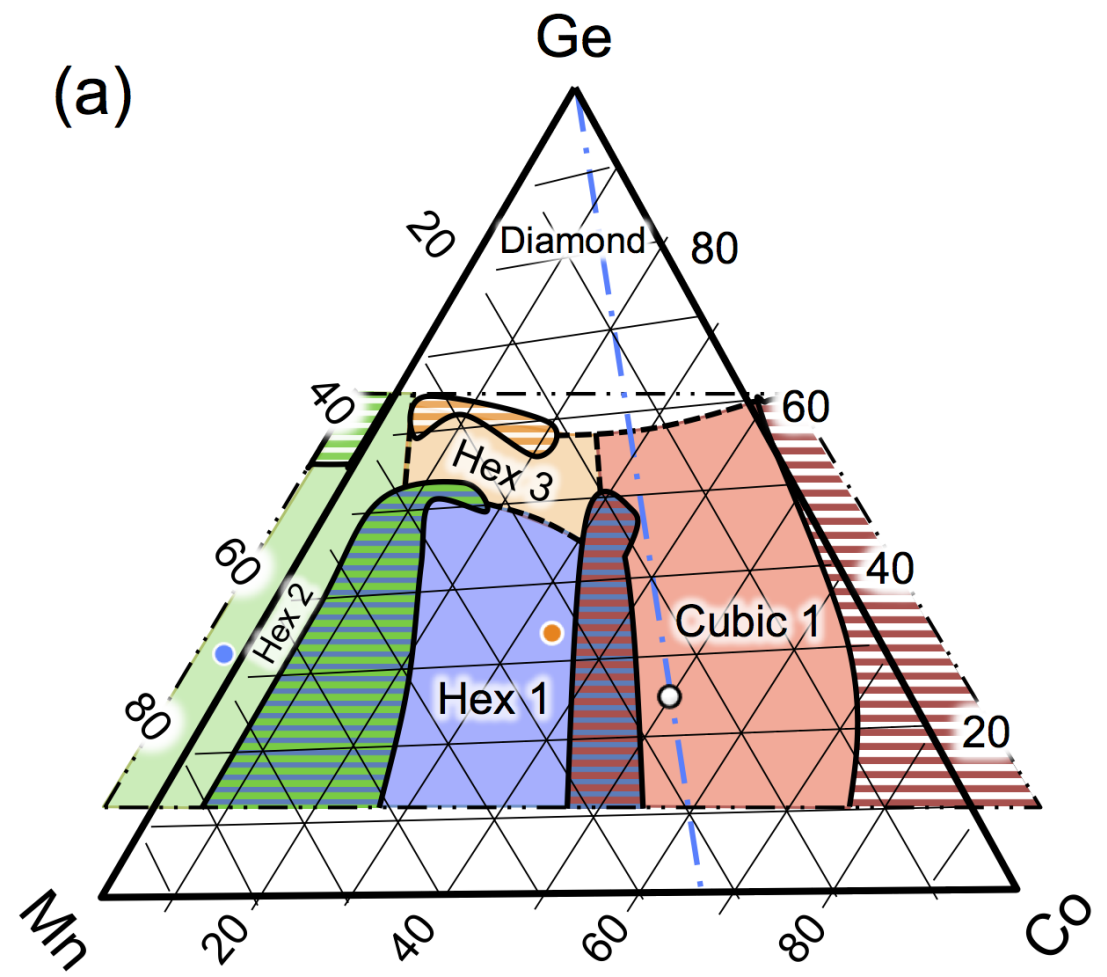
(a)
Ge
Mn
Co
Diamond
Hex 1
Hex 2
Hex 3
Cubic 1
20
40
60
80

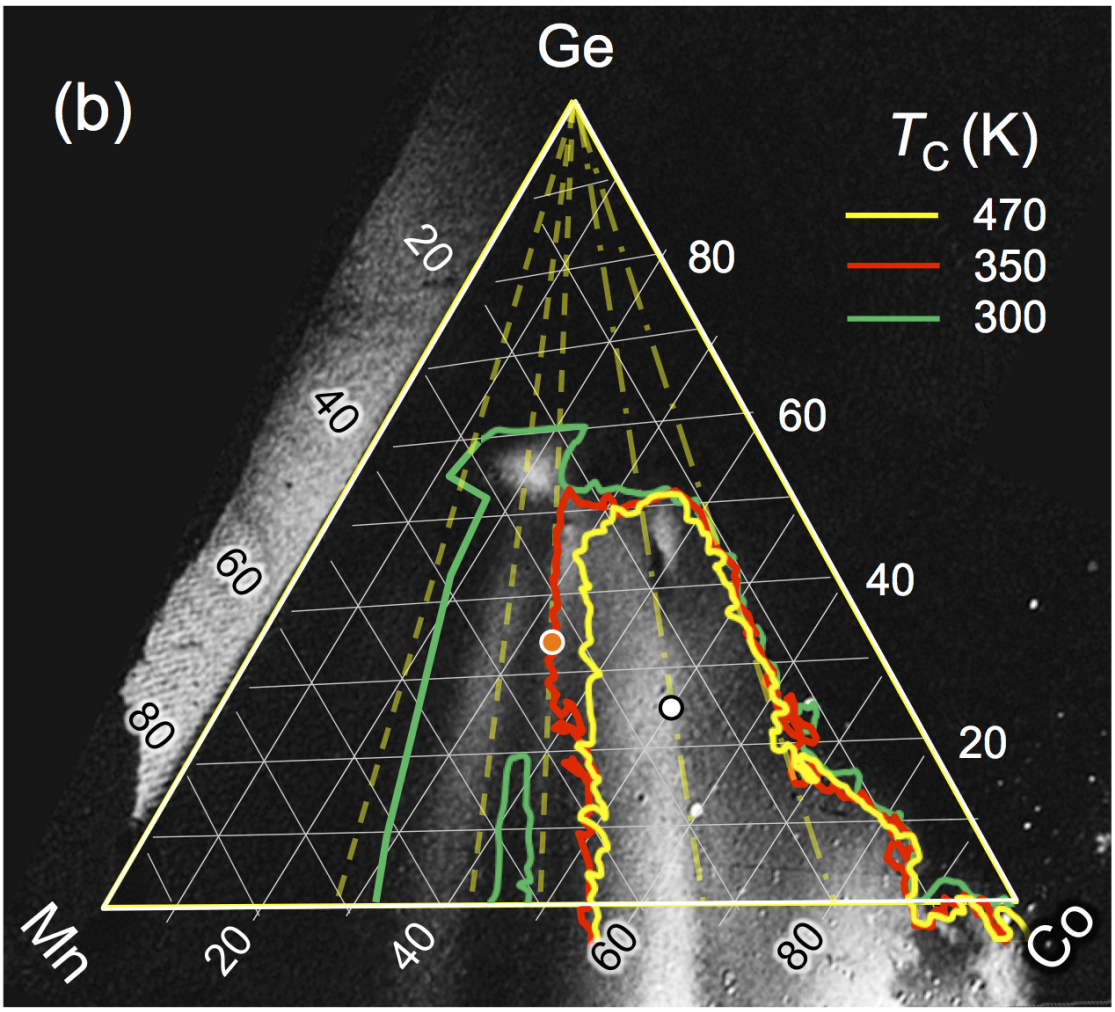
(b)
Ge
Mn
Co
T_C (K)
470
350
300
20
40
60
80

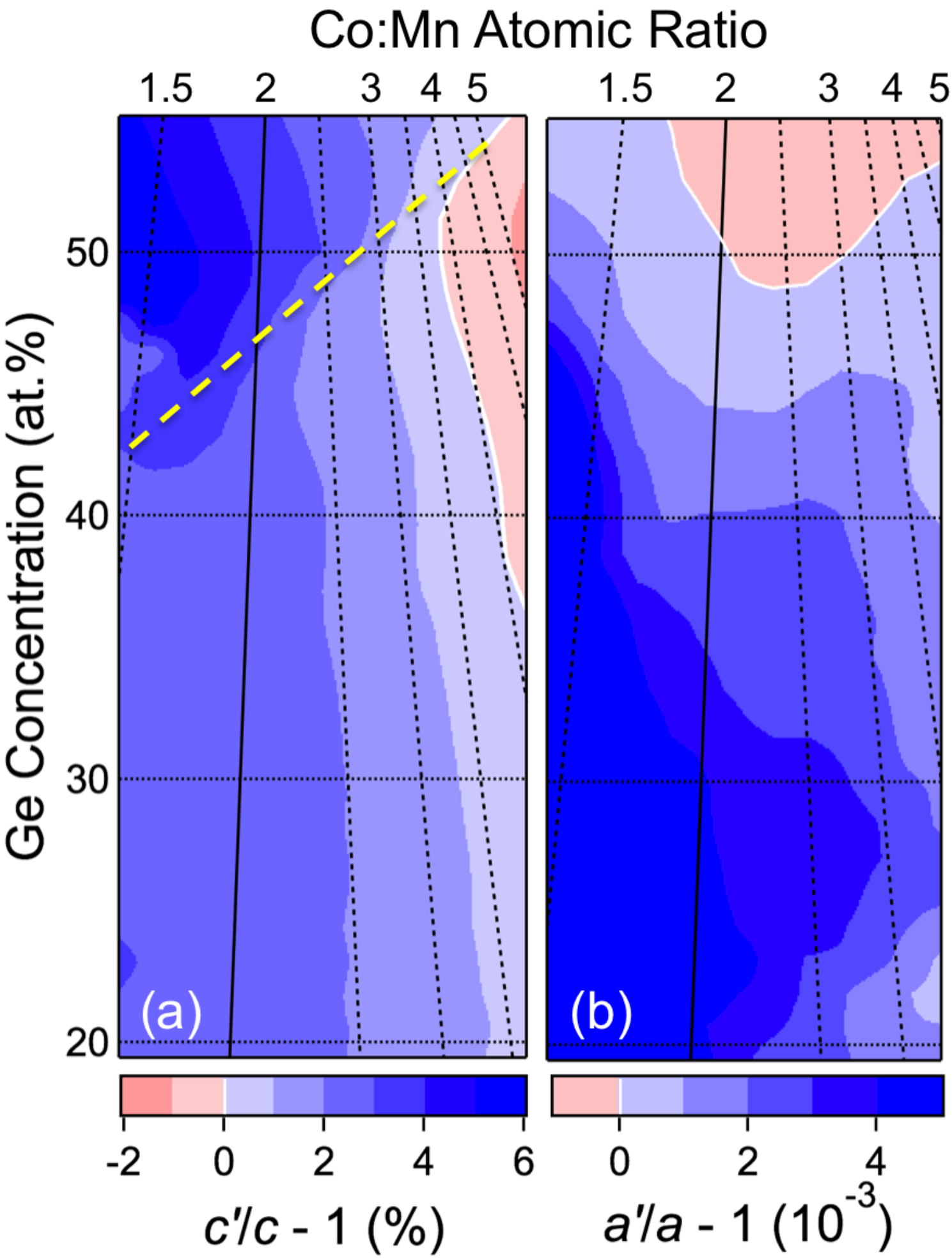
Co:Mn Atomic Ratio
1.5
2
3
4
5
Ge Concentration (at.%)
50
40
30
20
(a)
(b)
-2
0
2
4
6
c′/c - 1 (%)
0
2
4
a′/a - 1 (10-3)

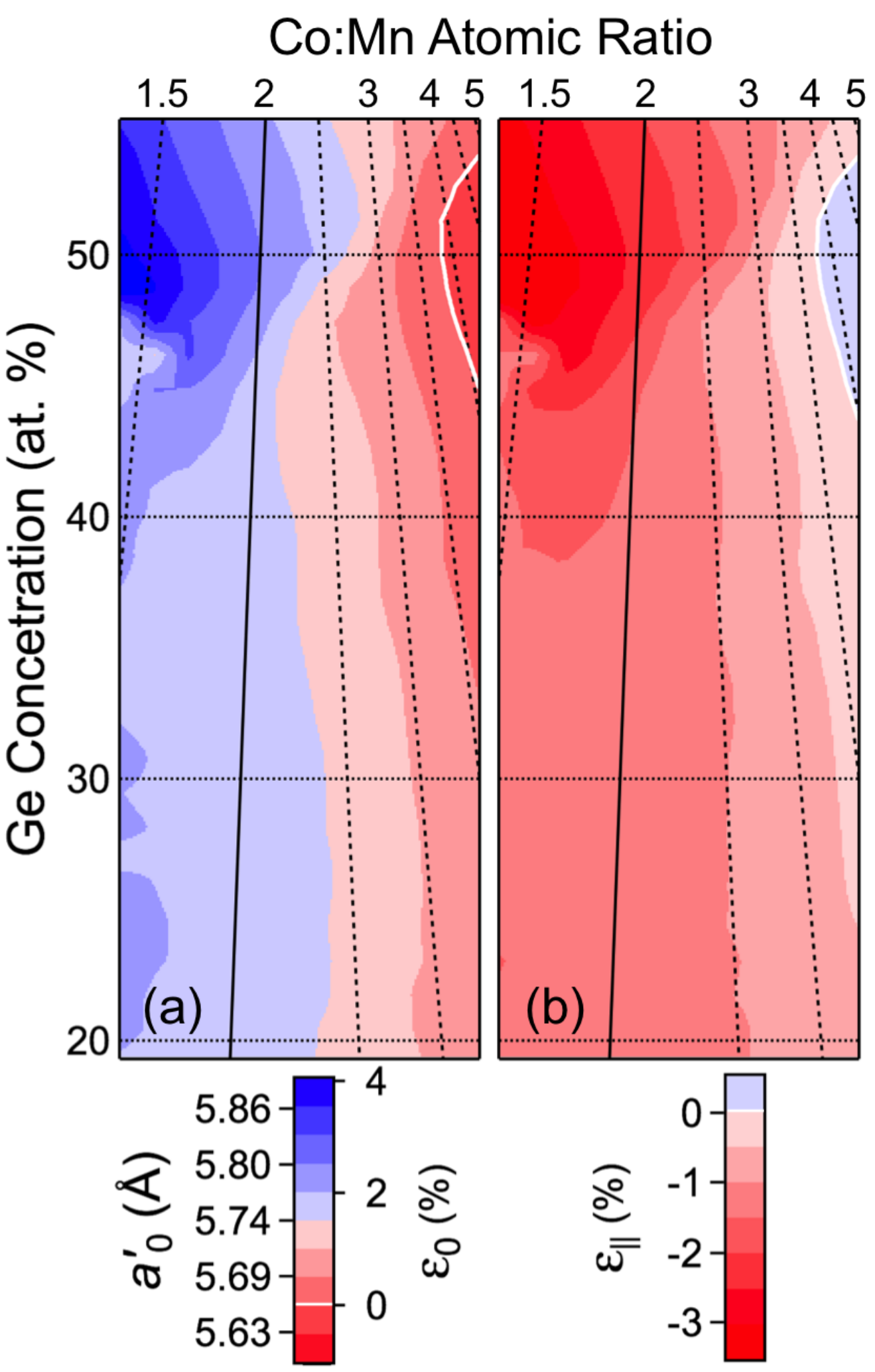
Co:Mn Atomic Ratio
1.5
2
3
4
5
Ge Concetration (at. %)
50
40
30
20
(a)
(b)
a'_0 (Å)
5.86
5.80
5.74
5.69
5.63
ε_0 (%)
4
2
0
$\varepsilon_{\parallel}$ (%)
0
-1
-2
-3

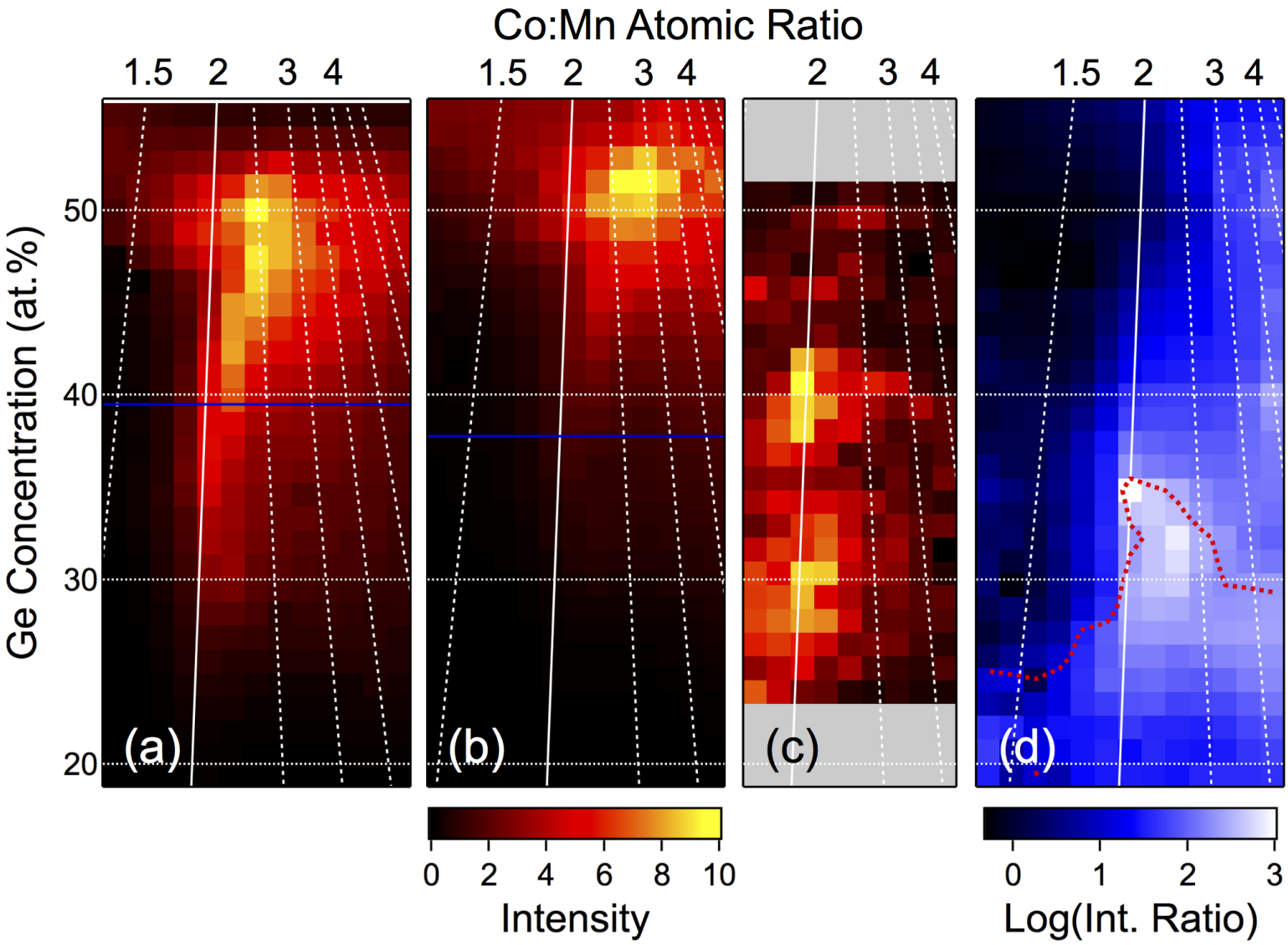
Co:Mn Atomic Ratio
1.5
2
3
4
Ge Concentration (at.%)
50
40
30
20
(a)
(b)
(c)
(d)
0
2
4
6
8
10
Intensity
0
1
2
3
Log(Int. Ratio)

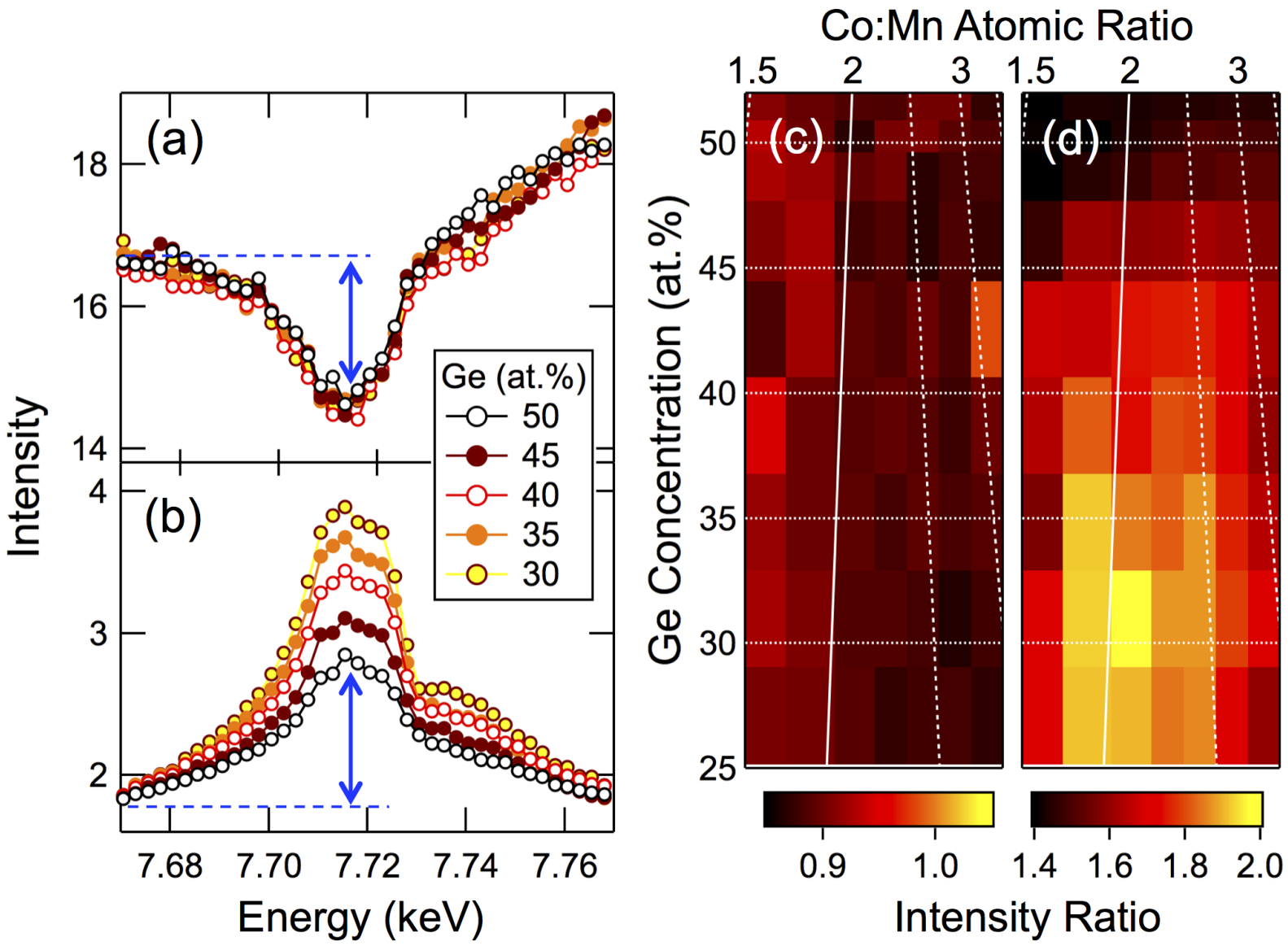
(a)
(b)
(c)
(d)
Intensity
Energy (keV)
7.68
7.70
7.72
7.74
7.76
18
16
14
4
3
2
Ge (at.%)
50
45
40
35
30
Co:Mn Atomic Ratio
1.5
2
3
Ge Concentration (at.%)
50
45
40
35
30
25
0.9
1.0
1.4
1.6
1.8
2.0
Intensity Ratio

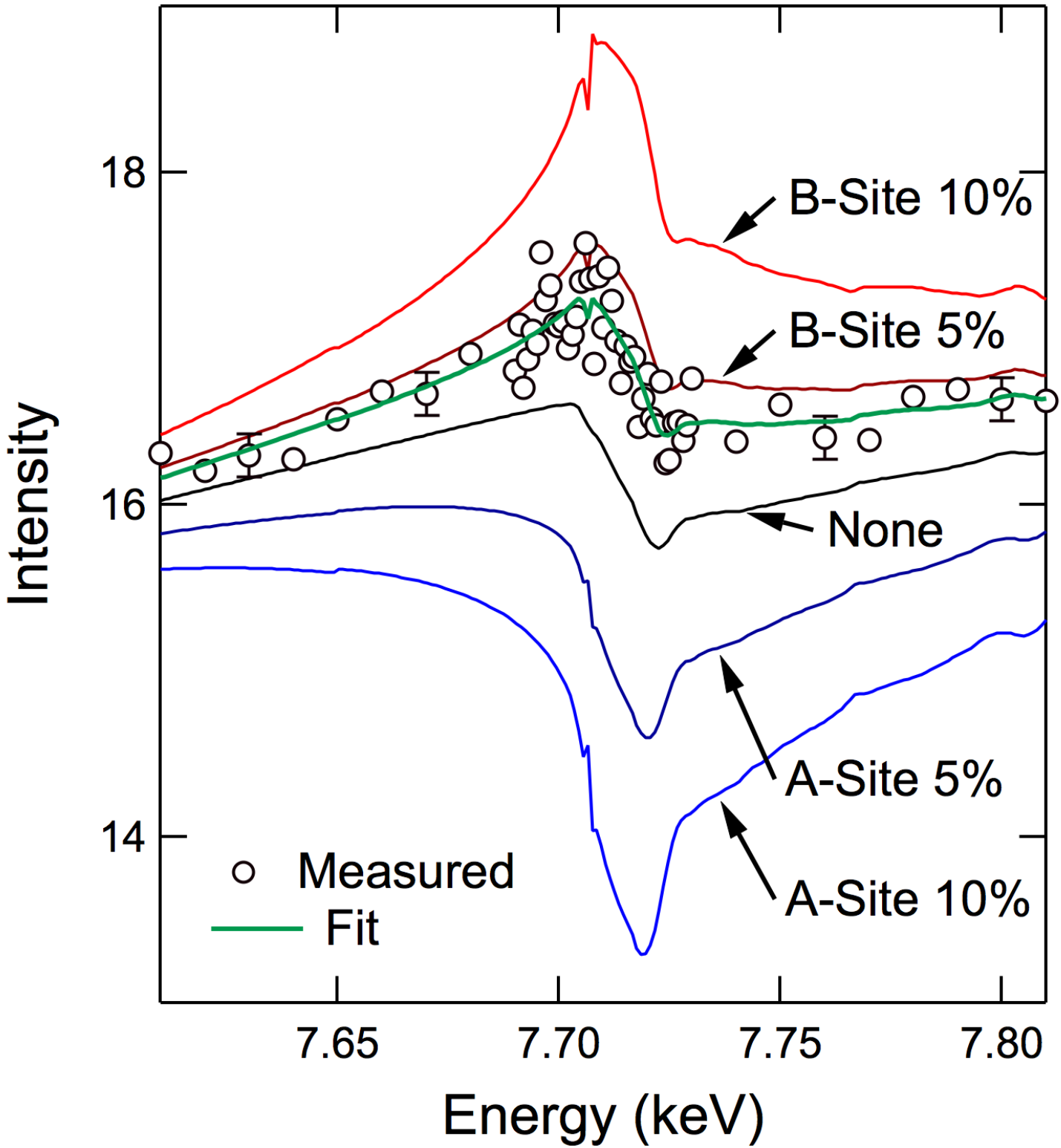
18
16
14
Intensity
B-Site 10%
B-Site 5%
None
A-Site 5%
A-Site 10%
Measured
Fit
7.65
7.70
7.75
7.80
Energy (keV)

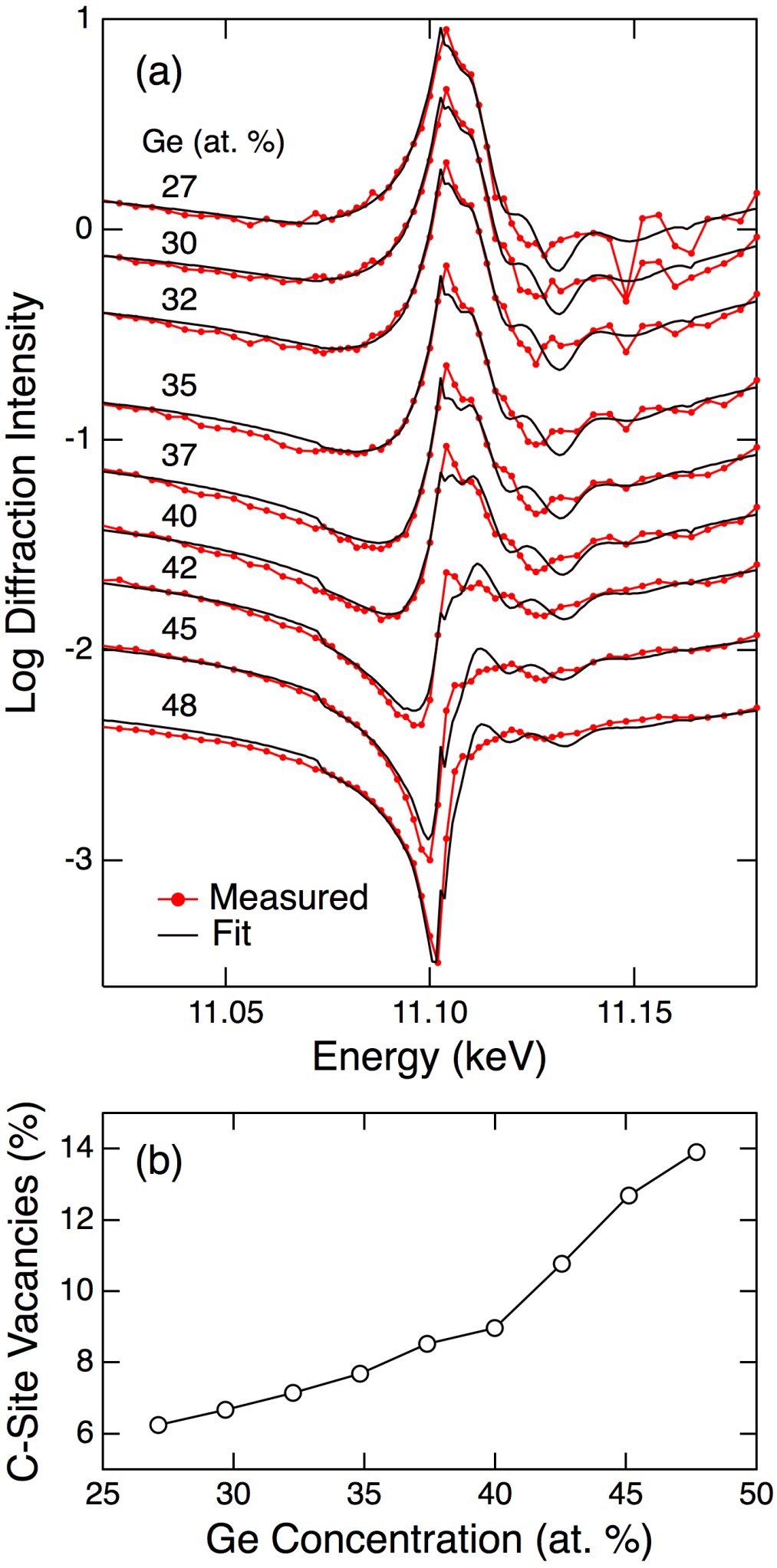
(a)
Ge (at. %)
27
30
32
35
37
40
42
45
48
Measured
Fit
Log Diffraction Intensity
Energy (keV)
1
0
-1
-2
-3
11.05
11.10
11.15
(b)
C-Site Vacancies (%)
Ge Concentration (at. %)
14
12
10
8
6
25
30
35
40
45
50

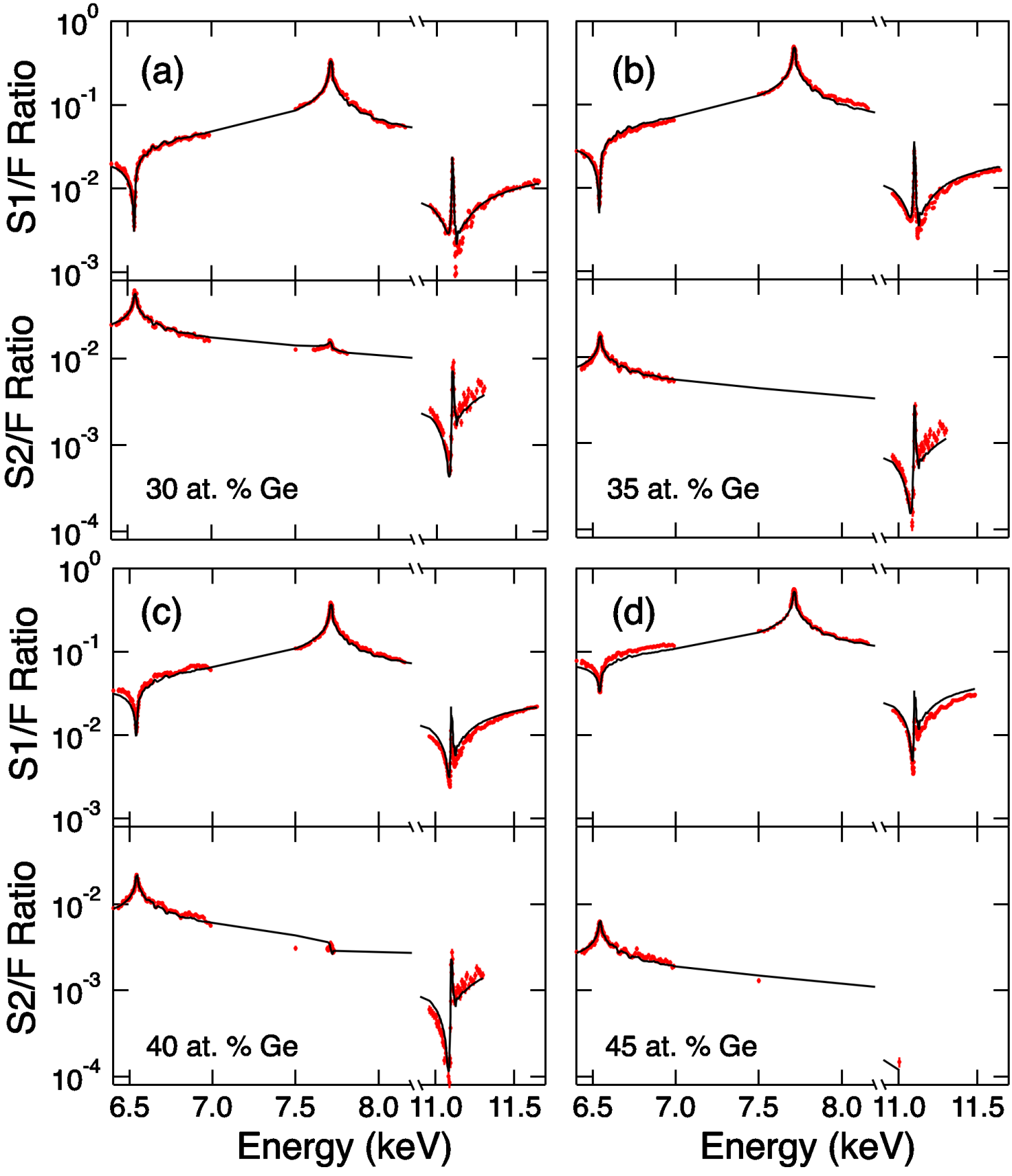
(a)
(b)
(c)
(d)
S1/F Ratio
S2/F Ratio
30 at. % Ge
35 at. % Ge
40 at. % Ge
45 at. % Ge
Energy (keV)
6.5
7.0
7.5
8.0
11.0
11.5

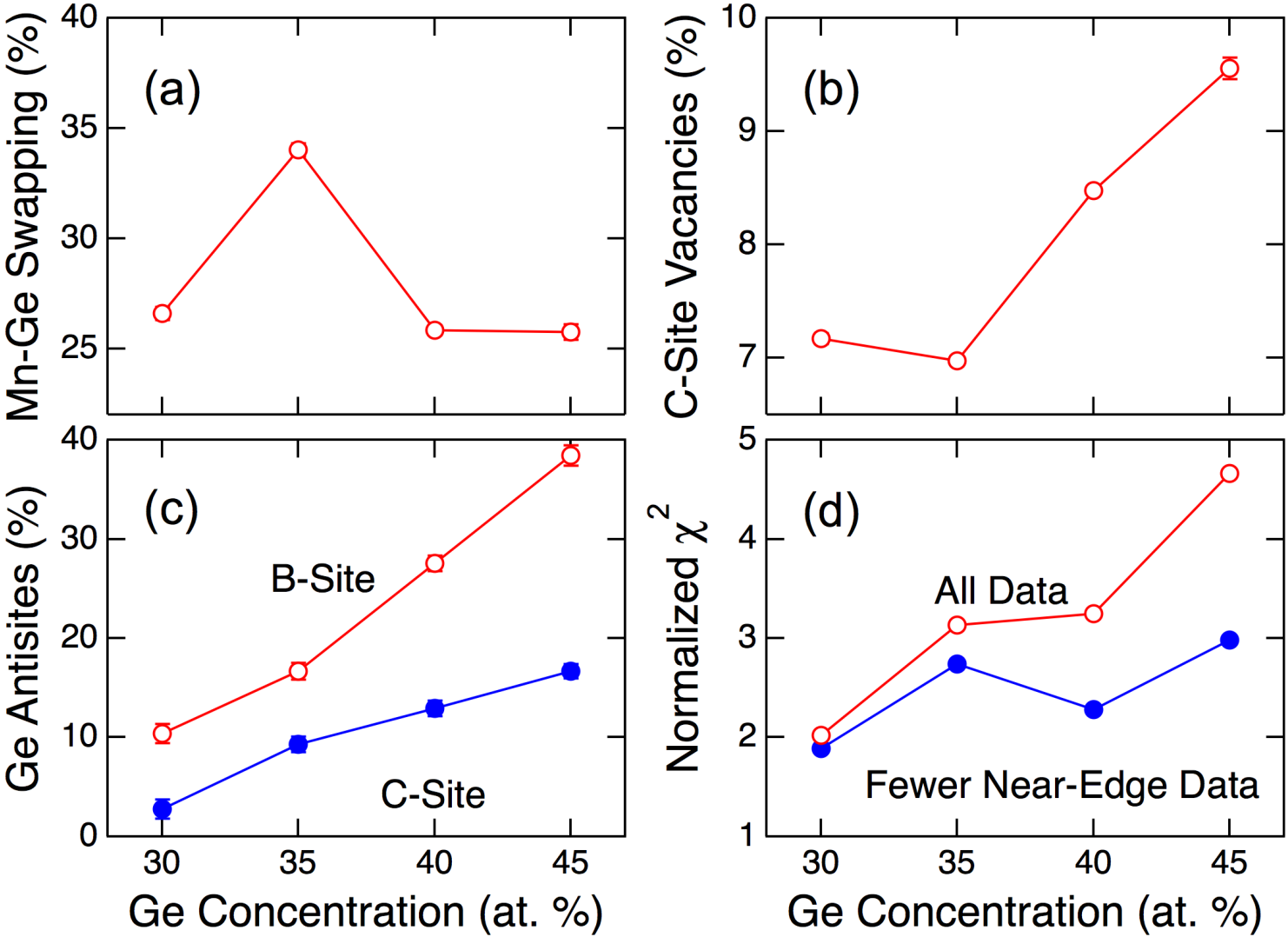
(a)
Mn-Ge Swapping (%)
40
35
30
25
(b)
C-Site Vacancies (%)
10
9
8
7
(c)
Ge Antisites (%)
B-Site
C-Site
40
30
20
10
0
30
35
40
45
Ge Concentration (at. %)
(d)
Normalized χ^2
All Data
Fewer Near-Edge Data
5
4
3
2
1
30
35
40
45
Ge Concentration (at. %)

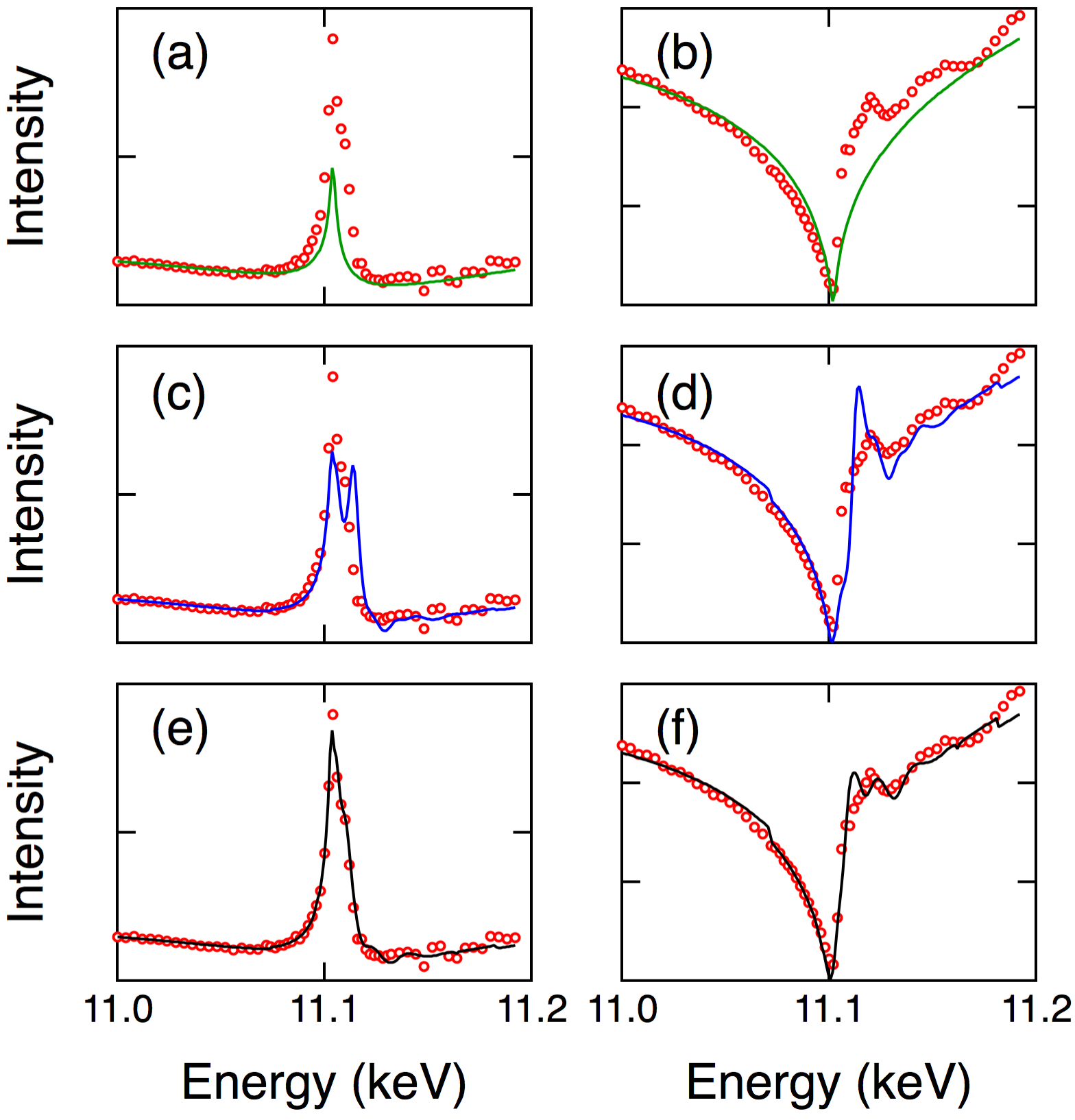
(a)
(b)
(c)
(d)
(e)
(f)
Intensity
Intensity
Intensity
11.0
11.1
11.2
11.0
11.1
11.2
Energy (keV)
Energy (keV)